NASA Technical Memorandum 83733

Summary of Recent NASA Propeller Research

Daniel C. Mikkelson, Glenn A. Mitchell,
and Lawrence J. Bober
Lewis Research Center
Cleveland, Ohio

Prepared for the
AGARD Fluid Dynamics Panel Meeting on Aerodynamics
and Acoustics of Propellers
Toronto, Canada, October 1-4, 1984

NASA

SUMMARY OF RECENT NASA PROPELLER RESEARCH

Daniel C. Mikkelson, Glenn A. Mitchell, and Lawrence J. Bober
National Aeronautics and Space Administration
Lewis Research Center
Cleveland, Ohio 44135

E-2216

SUMMARY

Advanced high-speed propellers offer large performance improvements for aircraft that cruise in the Mach 0.7 to 0.8 speed regime. At these speeds, studies indicate that there is a 15 to near 40 percent block fuel savings and associated operating cost benefits for advanced turboprops compared to equivalent technology turbofan powered aircraft. The current status of the NASA research program on high-speed propeller aerodynamics, acoustics, and aeroelastics is described. Recent wind tunnel results for five eight- to ten-blade advanced models are compared with analytical predictions. Test results show that blade sweep was important in achieving net efficiencies near 80 percent at Mach 0.8 and reducing near-field cruise noise by about 6 dB. Lifting line and lifting surface aerodynamic analysis codes are under development and some results are compared with propeller force and probe data. Also, analytical predictions are compared with some initial laser velocimeter measurements of the flow field velocities of an eight-bladed 45° swept propeller. Experimental aeroelastic results indicate that cascade effects and blade sweep strongly affect propeller aeroelastic characteristics. Comparisons of propeller near-field noise data with linear acoustic theory indicate that the theory adequately predicts near-field noise for subsonic tip speeds but overpredicts the noise for supersonic tip speeds. A study of advanced counter-rotation turboprops indicates that there may be about a 9 percent additional block fuel savings compared to a single rotation systems at Mach 0.8.

LIST OF SYMBOLS

A	noise amplitude
C_p	power coefficient = $P/\rho_o n^3 D^5$
CR	counter rotation
D	blade tip diameter, cm (in)
dB	decibel
$dC_p/d(r/R)$	elemental power coefficient $C_p = \int [dC_p/d(r/R)]d(r/R)$
FPS	velocity in units of feet per second
J	advanced ratio, V_o/nD
M	Mach number
MPS	velocity in units of meters per second
M_ℓ	local Mach number
M_o	free-stream Mach number
n	rotational speed, rpm
P	power, kW (ft-lb/sec)
R	blade tip radius, cm (in)
RPM	rotational speed, rpm
r	radius, cm (in)
SHP	shaft power, kW (hp)
SR	single rotation
T	thrust, N (lbf)
V_o	free-stream velocity, m/sec (ft/sec)
x	axial distance, cm (in)
$\beta_{3/4}$	propeller blade angle at 0.75 radius
η	efficiency = $(T \cdot V_o)P$
η_i	ideal efficiency = $(T_{ideal} \cdot V_o)P$
ρ_o	free-stream density, kg/m^3 ($slugs/ft^3$)
φ	phase angle
θ	ratio of total temperature to standard sea-level temperature of 518.7° R

INTRODUCTION

The free air propeller offers the potential of very high propulsive efficiencies for subsonic aircraft. This key propulsion component has been the object of many NACA/NASA research programs conducted throughout the history of the agency. From 1927 to about the mid 1950's NACA had an extensive propeller research effort. This research led

to many successful propeller powered aircraft with cruise speeds as high as Mach 0.6. From the mid 1950's to the mid 1970's there was about a 20-year hiatus in propeller research due to the success of turbojet and turbofan propulsion systems. These systems offered efficient flight at speeds from Mach 0.6 to 0.85 and cruise altitudes above most of the weather. The lower propulsive efficiencies of these systems compared to the early turboprops hardly mattered when the fuel costs were so low (near 10 cents per gallon). However, the world energy crisis of 1973 and 1974 changed all that and NASA began an initial modest effort to evaluate the need for a high-speed propeller research program. Both in-house and contractor studies indicated that at cruise speeds as high as Mach 0.8 an advanced high-speed turboprop powered aircraft would have a large performance advantage over an equivalent technology high bypass ratio turbofan. This superior performance could result in large block fuel savings, reduced life cycle costs, improved range, or other benefits for both future civil and military aircraft. To investigate these advantages a high-speed propeller research program was established at the NASA Lewis Research Center in 1976. This program has grown to encompass both experimental and analytical work into the aerodynamics, acoustics, and aeroelastics of advanced high-speed propellers. In the past, most of the research effort was directed toward developing advanced single-rotation propellers. More recently, however, the research work has been expanded to include advanced counter-rotation propellers which offer even higher performance potential. A possible future application of the technology from this program is illustrated by the photograph of Fig. 1 showing an advanced counter-rotation turboprop powered aircraft.

THEORETICAL ADVANTAGES OF TURBOPROPS

Propeller propulsion has some rather large efficiency advantages over more highly loaded propulsion systems. This can be shown by using simple momentum disk theory. Ideal propulsive efficiency is shown in Fig. 2 as a function of fan pressure ratio which is analogous to the commonly used propeller power loading (shaft horsepower divided by propeller diameter squared). These curves were derived for flight Mach numbers from 0.1 to 0.8 using simple momentum theory and represent only the losses associated with the acceleration of the fluid in the axial direction. The calculations assumed an adiabatic fan efficiency of 1.0 and included no viscous losses. The ranges in fan pressure ratio typical for each type of propulsor are indicated. Conventional low speed propellers generally are lightly loaded with fan pressure ratios up to about 1.03. Advanced propellers require more power to fly at higher speeds. Also, because of the low air density at the higher cruise altitudes, a higher power loading is required to keep the propeller diameter to a reasonable size. Fan pressure ratios for the higher-loaded advanced propellers will range from about 1.03 for single-rotation propellers of moderate loading to 1.10 for some of the more ambitious counter-rotation propeller designs. High bypass ratio turbofans are even more highly loaded with fan pressure ratios generally greater than 1.3.

The design point established for some initial advanced single-rotation turboprop engines included a power loading of 301 kW/m^2 (37.5 hp/ft^2) at 243.8 m/sec (800 ft/sec) tip speed and 10.668 km (35 000 ft) altitude. These conditions resulted in a design integrated fan pressure ratio of 1.047. The equivalent power loading of 301 kW/m^2 (37.5 hp/ft^2) is about three times the loading used on previous conventional propeller aircraft such as the Lockheed Electra/P-3. A typical advanced turbofan of comparable technology is projected to have a fan pressure ratio of about 1.6. Therefore (from Fig. 2) the ideal efficiency for the advanced turboprop at Mach 0.8 cruise would be 97 percent, while that for the comparable turbofan would be 80 percent. Thus, the turboprop exhibits an inherent 17 percent advantage. As seen in Fig. 2 this ideal advantage would be larger at lower flight speeds.

The simple momentum theory, however, does not account for the residual swirl loss in the wake of single-rotation propellers. This swirl is a loss that is unique to such propellers since it is not recovered by stators, as it would be in a fan engine or by a second rotor as it would be in a counter-rotation propeller. Therefore, the ideal propeller efficiency shown in Fig. 2 has to be corrected for this loss. The swirl loss is shown in Fig. 3 by comparing the basic axial momentum loss with the total induced loss for a configuration with an infinite number of blades. This loss is shown in Fig. 3 in terms of ideal propeller efficiency as a function of power loading. At the selected initial design power loading of 301 kW/m^2 (37.5 hp/ft^2) the swirl represents about a 7 percent performance penalty. However, it should be possible to eliminate this penalty if counter-rotation propellers are considered. This more mechanically complex approach is being investigated as an alternative propulsion concept in the NASA Advanced Turboprop Project (ATP) and will be discussed later in this paper.

A further efficiency correction for single-rotation propellers is the tip loss for a finite number of blades. Figure 3 shows that tip losses increase dramatically as the number of blades is reduced. At the higher power loadings the tip losses with two or four blades are excessive. With an eight blade propeller the tip losses are tolerable. For any number of blades, propeller efficiency increases as power loading is decreased. But such an increase in aerodynamic efficiency would require larger propeller diameters and thereby increase blade and gearbox weight. These considerations resulted in initial single-rotation propeller designs having eight blades and a power loading of 301 kW/m^2 (37.5 hp/ft^2). The tip loss for this design point is nearly 5 percent and the total loss (swirl and tip) above the axial momentum loss is about 12 percent. However, even with these two additional penalties, it is evident from Figs. 2 and 3 that the highly loaded single-rotation (SR) turboprop at Mach 0.8 still shows a significantly higher ideal efficiency than the high fan pressure ratio turbofan (85 percent versus 80 percent). As

is shown in the next section of this paper, this efficiency advantage for the turboprop would be even larger when comparisons include installed losses.

ADVANCED TURBOPROP POTENTIAL

A comparison of the installed cruise efficiency of turboprop-powered and turbofan-powered propulsive systems is shown in Fig. 4 over a range of cruise speeds. The efficiencies shown in the figure include the installation losses for both systems; namely, nacelle drag for the turboprop systems, and cowl drag and internal airflow losses for the fan stream of the turbofan systems. Conventional low speed turboprops have installed efficiency levels near 80 percent up to about Mach 0.5 but suffer from rapid decreases in efficiency above this speed due to increasing propeller compressibility losses. These losses are primarily the result of relatively thick blades operating at high helical tip Mach numbers.

The advanced high-speed turboprop has the potential to delay these compressibility losses to a much higher cruise speed and achieve a relatively high performance to at least Mach 0.8 cruise. Although high bypass ratio turbofans exhibit their highest efficiency at cruise speeds near Mach 0.8, their performance would still be significantly below that of the advanced turboprops. At Mach 0.8 the installed efficiency of turbofan systems would be approximately 63 percent compared to about 77 percent for the advanced single-rotation (SR) turboprop. Advanced counter-rotation (CR) high speed turboprops that recover the swirl losses would have an installed efficiency about 5 to 10 percent higher. At lower cruise speeds, the efficiency advantage of the advanced turboprop systems would be even larger.

A number of studies have been conducted by both NASA and industry to evaluate the potential of advanced high-speed turboprop propulsion for both civil and military applications. Numerous references to specific studies and summary results are listed in Ref. 1. The trip fuel savings trend shown in Fig. 5 plotted versus operating range is a summary of these studies. Installed efficiency levels similar to those shown in Fig. 4 for comparable technology advanced turboprops and turbofans were used in most of these studies. As shown in Fig. 5, trip fuel savings is dependent on aircraft cruise speed and range. At the bottom of the band, associated with Mach 0.8 cruise, fuel savings range from about 15 to 30 percent for advanced turboprop aircraft compared to equivalent technology turbofan aircraft. The larger fuel savings occur at the shorter operating ranges where the mission is climb and descent dominated. Because of the lower operating speeds encountered during climb and descent, turboprops have an even larger performance advantage than the advantage at Mach 0.8 cruise conditions. In a similar manner, a larger fuel savings is possible at Mach 0.7 cruise (represented by the top of the band in Fig. 5). At this lower cruise speed, fuel savings range from 25 percent to near 40 percent. Even larger fuel savings are possible by recovering the propeller swirl loss from these single-rotation turboprops. Counter-rotation is one promising concept for recovering swirl loss that is currently under investigation as part of the NASA Advanced Turboprop Project (ATP). Some results derived from a study of counter-rotation (Ref. 2) are shown in Fig. 5 for a 1300 nmi, Mach 0.8 counter-rotation turboprop aircraft. The gains in fuel savings over a single-rotation (SR) turboprop are of the same magnitude as the gains realized by reducing cruise speed from Mach 0.8 to Mach 0.7. This additional fuel savings gain projected for counter-rotation is about 8 to 10 percent.

ADVANCED DESIGN CONCEPTS

A model of an advanced high-speed SR turboprop propulsion system is shown in Fig. 6. The advanced propeller would be powered by a modern turboshaft engine and gear box to provide the maximum power to the propeller with a minimum engine fuel consumption. Propeller efficiency would be kept high by minimizing or eliminating compressibility losses. This would be accomplished by utilizing thin swept blades that would be integrally designed with an area ruled spinner and nacelle. Blade sweep would also be used to reduce noise during both take-off/landing and during high-speed cruise flight (Refs. 1, 3, and 4). Aircraft operations at high altitudes and Mach 0.6 to 0.8 requires much higher power than used on current propeller aircraft. A power loading about three to four times higher than existing technology low-speed turboprops would be needed to minimize propeller diameter and weight. Eight or ten blades are required to increased ideal efficiency at these higher disk loadings. In addition to these advanced concepts, a modern blade fabrication technique is needed to construct the thin, highly swept and twisted blades.

Since all of the advanced concepts used to minimize compressibility losses are interrelated, an integrated procedure is used to design high-speed propellers and nacelles (Refs. 1 and 5). The effects of applying these advanced concepts to a propeller design are shown in Fig. 7. This figure is based on a cruise condition of Mach 0.8 and shows the propeller blade Mach number as it varies from hub to tip. The Mach number at each radial location is called the section Mach number and is the vector sum of the axial and rotational components. Curve A represents the Mach number distribution encountered by the propeller operating in an unsuppressed flow field where the axial component is the free-stream Mach number. At the hub the section Mach number is slightly higher than the cruise speed of Mach 0.8. As the rotational velocity component becomes larger at increased radius, the relative Mach number increases until it reaches Mach 1.14 at the blade tip. This Mach number must be compared to the drag rise (or drag divergence) Mach number of each blade airfoil section to evaluate the propeller performance potential. The predicted drag rise Mach number (Fig. 7, curve B) was obtained from isolated two-

dimensional airfoil data for a high-speed propeller having thickness-to-chord ratios of about 15 percent at the hub and 2 percent at the blade tip. Across the entire radius the section Mach number (curve A) is higher than the drag rise Mach number (curve B). This represents a potentially large compressibility loss.

The advanced aerodynamic concepts of thin swept blades and an area ruled spinner and integrated nacelle design are effective in minimizing or eliminating these losses. In the outer portions of the propeller, the thin blades are swept to reduce the component of velocity normal to the blade airfoil section, similar to swept wing theory. With a sufficient amount of sweep the section Mach number (curve A) can be reduced to an effective Mach number (curve C) that is below the drag rise Mach number (curve B) in the outer portions of the blade. This procedure significantly reduces the compressibility losses in the blade tip region and can also be effective in reducing noise. In the hub region, the spinner-nacelle body is tailored to increase the effective nacelle blockage behind the propeller and reduce the local Mach number through the propeller plane. This effect is shown by the local surface Mach number distribution plotted for the spinner-nacelle body in Fig. 7 (without blade blockage effects) and the resulting effective section Mach number of curve D. Near the hub the effective section Mach number is suppressed far below the drag rise Mach number. With a large number of blades (8 in this example), the hub blade sections operate as a cascade and the additional Mach number suppression is necessary to prevent blade-to-blade choking. Area ruling the spinner between the blades gives further relief from choking by opening the flow area between the blades at the spinner.

In addition to maximizing the aerodynamic performance of the advanced turboprop, techniques for minimizing the near-field source noise during cruise operation have been developed to keep interior noise levels competitive with current wide body aircraft and to minimize the need for fuselage acoustic treatment. Since the blade relative tip Mach numbers are slightly supersonic as shown in Fig. 7 ($M_{TIP} \sim 1.14$) the initial approach for noise reduction was to add sweep and reduce the effective local section Mach number to below the section critical Mach number. The shock strength and, therefore, the resulting pressure pulse is thereby reduced. The initial blade designs with 30° tip sweep were expected to be somewhat quieter for this reason. A more advanced concept was incorporated in a 45° tip sweep design using the linear acoustic analysis of Ref. 6. A historical development of the application of acoustic theory to advanced propeller design is given in Ref. 7. The present theory predicts thickness (due to blade airfoil thickness distribution) and loading (due to pressure loads on the blade airfoil) noise components from each radial section of the blade. Thickness noise is generally the dominant noise source on a propeller operating with a slightly supersonic tip Mach number. By properly sweeping and stacking the blade it is possible to reduce near-field noise using the phase interference concept illustrated in Fig. 8. The noise from one propeller blade is the vector sum of the contributions of the sinusoidal wave (amplitude and phase angle) from each radial strip. The noise of the total propeller is the product of the vector sum and the number of blades. Sweeping the tip back causes its signal to lag the signal from the mid-blade region. This increase in phase angle causes partial interference and a reduction in noise. This phase interference concept was used in the acoustic design of the 45° swept propeller model (SR-3, Fig. 9) to reduce the near-field cruise noise. This concept should have application to both thickness and loading noise in the near and far fields.

PROPELLER MODEL DESIGNS

In a cooperative program between NASA Lewis Research Center and Hamilton Standard the concepts described above were used to design a series of propeller models for wind tunnel testing. The basic blade planforms pictured in Fig. 9 represent five propeller designs that have been wind tunnel tested. All of the propellers shown in the figure except the fourth one (SR-6) were designed by Hamilton Standard. The SR-6 was aerodynamically designed at the Lewis Research Center. The first three propellers shown in the figure (SR-2, SR-1M, and SR-3) have a blade tip speed of 244 m/sec (800 ft/sec), a cruise power loading of 301 kW/m^2 (37.5 hp/ft^2) at Mach 0.8 and 10.668 km (35 000 ft), and eight blades. The last two propellers shown are ten-bladed models. The SR-6 has a design blade tip speed of 213 m/sec (700 ft/sec), and a cruise power loading of 241 kW/m^2 (30 hp/ft^2); and the SR-5 has a design blade tip speed of 183 m/sec (600 ft/sec) and a cruise power loading of 209 kW/m^2 (26 hp/ft^2). The blade planforms are identified by tip sweeps of 0°, 30°, 45°, 40°, and 60°. Here the tip sweep is approximately the angle between the blade mid-chord line at the tip of the blade and a radial line intersecting this line at the tip.

The straight blade and an initial 30° swept blade (not shown) were designed using established analyses (Ref. 8) that lack a refined methodology to design the twist of a swept blade. Tests of the initial 30° swept design indicated a retwist was required (which was actually a redistribution of the blade load from hub to tip). That became the modified 30° swept design shown in Fig. 9 (SR-1M). The 45° and 60° swept blades (SR-3 and SR-5) were designed for acoustic suppression as well as improved aerodynamic performance by tailoring the sweep and planform shape as described in Ref. 9. The Lewis propeller design (SR-6) was based on a different design philosophy, wherein the cruise design conditions were changed from those used for the first three propellers in order to increase predicted performance and lower noise. The design tip speed of this propeller was lowered to help reduce noise. The predicted performance lost by the lower tip speed was regained and possibly increased slightly by increasing the number of blades to 10 and lowering the power loading to 241 kW/m^2 (30 hp/ft^2). The technique of lowering tip speed and power loading was also used with the SR-5 design. Its design point was

chosen to further reduce noise and obtain about the same predicted performance level as the eight-bladed models. More detailed discussions of the aero/acoustic design methodology represented by the SR-3 and SR-5 designs are presented in Refs. 6, 7, and 10.

The noise levels that were predicted at the time these blades were designed are listed in Fig. 9. The cruise noise predictions indicated a small reduction for 30° of sweep, a significant reduction for the aero/acoustic 45° swept design and the 40° ten-bladed design and a very large reduction for the 60° ten-bladed design.

Each photograph in Fig. 10 shows one of the five propeller models that was installed on the Propeller Test Rig (PTR) in the NASA Lewis 8- by 6-Foot Wind Tunnel. The tunnel (Ref. 11) has a porous wall test section to minimize any wall interactions. The PTR is powered by a 746 kW (1000 hp) air turbine using a continuous flow 3.1×10^6 N/m^2 (450 psi) air system routed through the support strut. Axial force and torque on the propeller are measured on a rotating balance located inside of an axisymmetric nacelle behind the propeller (Ref. 9). The propeller diameters range from 0.622 m (24.5 in) to 0.696 m (27.4 in).

PROPELLER AERODYNAMIC RESEARCH

Experimental Research

Experimental wind tunnel test results obtained with the eight-bladed propellers (Refs. 1, 5, 9, and 12) are summarized in Fig. 11. The net efficiencies of the 0°, 30°, and 45° swept blade designs are shown for Mach numbers from 0.6 to 0.85. Because the power coefficient and advance ratio are constant in this figure, the ideal efficiency is also constant as is shown by the upper dashed line. The ideal efficiency represents the performance of an optimally loaded propeller with no blade drag. The difference in Fig. 11 between the ideal efficiency line and the experimental performance curves represents viscous and compressibility losses, possible hub choking losses, and losses associated with a nonoptimum radial loading distribution. As the data curves show, those losses increase at the higher speeds due to increasing compressibility losses. However, the performance of the 45° swept blade decreased a smaller amount with increasing speed than the performance of propellers with less sweep. The 45° swept blade achieved a 3 percent performance gain over the straight blade design at Mach 0.8 and about a 4 percent gain at Mach 0.85. At the lower speeds of Mach 0.6 to 0.7 both swept blades had approximately a 2 to 3 percent efficiency advantage over the straight blade and the highest performing design had an efficiency that exceeded 81 percent. At speeds near Mach 0.6 the straight blade design may not have had an optimum twist distribution. Unpublished data with an identical blade shape constructed from graphite rather than steel (that apparently deflected to a more optimum twist distribution) had a net efficiency near the 45° swept design at Mach 0.6. The study level (shown on Fig. 11) of 79.5 percent efficiency at Mach 0.8 was the value used in projecting the large fuel efficiency and operating cost advantages of an advanced turboprop over an equivalent technology turbofan powered aircraft. The 45° swept propeller at this speed had an efficiency of 78.7 percent which was close to this study level.

By operating the eight-bladed 45° swept propeller at off design lower power loadings, higher efficiencies can be obtained at Mach 0.8. This is shown in Fig. 12 where net efficiency is plotted against advance ratio for several levels of power loading. The typical variation of efficiency with advance ratio at a constant power loading (i.e., constant C_p/J^3) is a peaked curve. The reduction from the peak with increasing advance ratio is due to (1) a combination of lower ideal efficiencies due to increased swirl and tip losses and (2) lower blade sectional lift to drag ratios (from increasing local angles-of-attack). The fall-off with decreasing advance ratio is due to increased compressibility losses associated with the higher tip rotational speeds and/or again lower blade section lift to drag ratios (from decreasing local angles-of-attack). The circle symbol in Fig. 12 represents the eight-bladed 45° swept propeller design point. The square symbol on the 80 percent power loading curve shows the design power loading and advance ratio of the ten-bladed 40° swept propeller (SR-6). The effect of operating the eight-bladed 45° swept propeller at this reduced power loading and increased advance ratio (3.06 to 3.5) was to increase efficiency about 0.3 percent. This reduced power loading would result in a 12 percent larger propeller diameter in an actual aircraft installation where power requirements are fixed. The eight-bladed 45° swept propeller obtained an efficiency of 79.7 percent at 80 percent power loading and 3.3 advance ratio and an efficiency slightly above 80 percent at 70 percent power loading.

A comparison of the eight- and ten-bladed propellers (Ref. 13) is shown in Fig. 13 where net efficiency is plotted versus Mach number. These data show both propellers operating at the ten-bladed propeller design power coefficient and advance ratio. The performance of the ten-bladed propeller was about 3/4 to 1 percent higher than that of the eight-bladed model from Mach 0.6 to Mach 0.75. This higher performance would be expected due to the higher ideal efficiency for a blade count increase from 8 to 10. For the eight-bladed propeller, the performance loss due to compressibility effects began above Mach 0.7 and increased gradually with increasing speed. The ten-bladed propeller, however, showed no performance loss up to a speed near Mach 0.75. Beyond this speed, the efficiency fell rapidly with increasing Mach number. By Mach 0.8, the efficiency had fallen 3 percent and was 1/2 percent below the eight-bladed model.

Since the rapid performance loss of the ten-bladed, 40° swept propeller was believed to be due to the onset of choking in the interblade region near the hub, a new flow visualization technique, called the paint flow technique, was developed and used to

determine the extent of interblade choking (Refs. 14 and 15). The paint flow technique consists of painting the propeller blades with a red undercoat and a white overcoat. Then with the propeller operating at the desired test condition, an upstream jet atomizer was turned on to produce a cloud of dioctyl-phthalate (DOP) particles. The DOP solvent then impinged on the rotating propeller blades and after about 30 min of testing caused the paint to flow, etching the surface airflow patterns into the surface of the blades.

The results of these paint flow tests with the ten-bladed propeller operating near design conditions at Mach 0.8 is shown in Fig. 14. The photographs indicate a rather extensive shock on both the pressure and suction sides of the propeller blade. The shock structure extends far from the hub region to near the blade mid-radius. The extensive shock structure indicates that hub choking was quite severe, and propagated outward over a considerable portion of the blade span. A low hub-to-tip ratio together with close blade spacing reduced the interblade flow area on this ten-bladed propeller and contributed to the choking problem. In addition, the larger propeller diameter of this model (0.696 m (27.4 in) compared to 0.622 m (24.5 in) for the SR-3) increased the blade root chord, and structural constraints prevented thinner root sections. Future efforts in spinner area ruling techniques (Ref. 8) to reduce the interblade root Mach number in combination with advanced controlled diffusion cascades, and the use of lighter, structurally superior, advanced composite blade material to achieve thinner root sections may be able to minimize these root section design problems.

Analytical Research

Advanced aerodynamic analysis methods for predicting high-speed propeller performance are being developed as a part of the NASA Propeller Research and Advanced Turboprop Programs (Ref. 8). The analysis methods (Fig. 15) range from simple short running lifting line programs such as the existing strip analysis for single-rotation propellers based upon Goldstein's work (Ref. 16) to very complex long running programs such as the lifting surface analysis that solves the five Euler equations (Refs. 17 to 19).

The existing Goldstein type strip analysis assumes the vortex wake is composed of a rigid helical vortex sheet, corresponding to the optimum span-wise loading of a lightly loaded propeller. The propeller is restricted to having straight blades and there is no provision for a nacelle since the vortex wake extends to the axis. Simple modifications have been made to existing analyses in an attempt to circumvent these restrictions. For example, the simple cosine rule is used to account for blade sweep and a radial gradient of axial velocity is used to account for the effect of the nacelle.

More recent lifting line analyses, such as the curved lifting line program (Ref. 20) and the propeller nacelle interaction program (Ref. 21) include a swept lifting line capability, and to varying degrees, the ability to account for the presence of the nacelle in the analysis.

The curved lifting line analysis represents the wake by a finite number of helical vortex filaments instead of the continuous sheet of vorticity used by Goldstein. Each filament has a constant pitch, but its location relative to the other filaments is arbitrary. The strengths of the individual wake filaments are related to the spanwise variations of the bound vortex strength. Since both of these are unknown, the blade and wake vortex strengths are solved simultaneously. This solution is made possible by placing the bound vortex along the quarter chord line and requiring the flow to be tangent to the blade mean camber line along the three-quarter chord line. With these conditions, the blade and wake vortex strengths can be computed. The lift coefficient of the blade at any radial location is then determined from the bound vortex strength at the same radius. Drag is provided by correlated two-dimensional airfoil data. The total induced velocity at any point in the flow field is obtained by summing the induced flow of the bound vortex and the trailing vortex system. In this analysis, the propeller blades are represented by curved lifting lines which can have any arbitrary shape. The nacelle shape is an infinite cylinder since the wake filaments cannot contract radially. However, a radially varying propeller inflow velocity can be accounted for. This analysis was originally applicable only to single-rotation propellers, but has now been recently extended to include counter-rotation propellers.

The propeller nacelle interaction analysis (Ref. 21) also represents the wake by a finite number of vortex filaments. However, this analysis allows the vortex filaments to be placed along stream surfaces so that they conform to the shape of an axisymmetric nacelle. This is accomplished in the analysis by the calculation of the inviscid flow around the nacelle alone, which locates the wake vortex filaments around the nacelle and determines the radial variation of the inflow velocity at the propeller. The induced velocity is determined by summing the induced flow from the individual filaments and the swept lifting line. The local blade lift and drag are determined from two-dimensional airfoil and cascade data contained in the program and the calculated local blade angle of attack. An optional step in the analysis allows the calculated blade forces to be used in a circumferentially averaged (axisymmetric) viscous compressible flow calculation to determine interblade and off-body velocities. This calculation can indicate whether the velocities are high enough to result in large shock wave losses, and can determine the drag of the nacelle in the presence of the propeller. The wake model in this analysis can be applied to both single and coaxial counter-rotation propellers. The propellers can have blades of any arbitrary shape and the nacelle can be any axisymmetric geometry.

Finite difference lifting surface analyses that can solve the complete three-dimensional flow field are also under development. These analyses require the generation of a complex grid system which conforms to the shape of the nacelle and propeller. The nacelle shape is required to be axisymmetric so that the flow between each two adjacent blades is the same, and it is only necessary to solve for the flow between two blades. Beyond the tips and upstream and downstream of the blades, the flow is assumed to be periodic. On all solid surfaces the flow is required to be tangent to the surface.

One lifting surface inviscid analysis that is under development for single-rotation propellers solves the single full transonic potential equation (Ref. 22). It requires the wake location to be defined and does not account for shock total pressure variation although it indicates the shock location. Another lifting surface technique is the Euler analysis (Refs. 18 and 19) which is being developed for both single- and counter-rotation propellers. The equations used in the Euler analysis are the five unsteady three-dimensional Euler equations. These govern the inviscid flow of a compressible fluid and can accurately represent the total pressure variation caused by shock waves and the work done by the propeller. This analysis requires no wake modeling and no two-dimensional airfoil data. This code has a significantly longer running time than the transonic potential analysis. These lifting surface analyses will be able to predict detailed pressure distributions on both sides of the propeller blade as well as the flow conditions in any portion of the off-body flow field.

The final type of analysis under development utilizes the time averaged Navier-Stokes equations. This analysis also does not require the wake location to be specified. Since this analysis includes viscous effects in the governing equations, it can predict important features of the flow not addressed by the inviscid analyses. These include details of the blade and nacelle boundary layers, blade tip flow, blade-nacelle corner flow and blade viscous wakes.

Such detailed three-dimensional results will be important tools for improving the aerodynamic, acoustic and structural performance of propellers through a better understanding of the complicated flow processes of advanced high-speed propellers.

Experimental to Analytical Comparisons

Although these lifting line and lifting surface programs are still under development, some comparisons of their results with wind tunnel experimental data obtained with a laser velocimeter (LV), a rotating force/torque balance and a flow survey probe on an eight-bladed, 45° swept propeller (SR-3) have been made (see also Ref. 23). These comparisons are intended to show the current status in the development of the programs.

The first analytical/experimental data comparisons were made with wind tunnel experimental data obtained using the laser velocimeter (LV) system. The laser velocimeter system was developed to obtain nonintrusive measurements of detailed velocities ahead of, in between, and behind propeller blades (Refs. 24 to 26). The laser system is shown in Fig. 16 installed in the NASA Lewis 8- by 6-Foot Wind Tunnel. The SR-3 propeller, spinner, and nacelle can also be seen in this figure.

This laser velocimeter system uses a 15-W argon ion laser which is operated at about one-third power. The system uses a four beam on-axis backscatter optic system. The measuring volume is moved axially and vertically within the wind tunnel by traversing the entire laser system and is moved horizontally by using a zoom lens assembly. The movement of the measuring volume is remotely computer controlled. The flow within the tunnel is artificially seeded with dioctyl phthalate (DOP). The four beam laser velocimeter is capable of measuring two velocity components simultaneously. The four beams were set up such that the planes defined by the two beams of each color were essentially orthogonal to each other and at nominally 45° to the horizontal plane of the wind tunnel. The axial and tangential components of velocity were obtained by making a measurement in the horizontal plane which passes through the propeller rotational axis. The axial and radial components of velocity were similarly obtained by making measurements in the vertical plane which passes through the rotational axis.

In Fig. 17, the laser velocimeter velocity data is compared with results from the curved lifting line analysis. The comparisons shown are for the eight-bladed, 45° swept (SR-3) propeller (shown in Fig. 16) operating at a tunnel Mach number of 0.8, a design advance ratio of 3.06, a corrected tip rotational speed ($V_t/\sqrt{\theta}$) of 280 m/sec (917 ft/sec), a helical tip Mach number of 1.15, a power coefficient of 1.8, and a blade angle setting at the three-fourths radius of 60.5°.

A color computer graphic technique similar to Refs. 27 and 28 was utilized to evaluate and compare the measurements and predictions of the highly three-dimensional exit flow from the propeller. At an axial station just behind the propeller, laser velocimeter (LV) circumferential surveys were taken at 17 radial positions located from 59 to 122 percent of the blade span. These data were used to generate the computer graphic presentations of Fig. 17 where shades of gray replace the color coding presented in Ref. 26. At each radial position, the data over the complete circumference for the eight blades was folded to a 45° segment to provide data in a single equivalent blade passage. The circumferential data was averaged to provide 30 circumferential values within this "equivalent" blade passage. The entire array of experimental data at 17 radial positions by 30 circumferential positions was interpolated to provide data at intermediate positions, color-coded and displayed on a color raster display. The

results were photographed and then reprocessed to gray shades to provide the results shown in the figure. The analytical results were processed in an identical manner. Velocities were predicted for the same 17 by 30 array of spatial positions, computer interpolated and graphically displayed.

Figure 17 presents the axial velocity field in the absolute reference frame seen by a stationary observer. The blade rotation in the figure is in the counterclockwise direction when viewed from behind the propeller looking forward. The axial velocity measured by the laser velocimeter clearly show the thick blade wakes and the tip vortex. The light gray region adjacent to the blade wakes is the high velocity from the suction surface. The maximum suction surface velocity occurs at about 0.9 of the tip radius. In making the comparison of the LV data with the results from the curved lifting line analysis, the viscous blade wakes must be ignored since they are not included in the analysis. The comparison also shows the analysis has a stronger predicted tip vortex because of the mathematical singularity present in the analysis at the tip. The general character of the flow field as measured is strikingly similar to the flow field predicted by the curved lifting line analysis. Some flow disturbances are noted beyond the blade tip. These velocity fluctuations may present a potential noise source. In general, the curved lifting line analysis shows good qualitative agreement with the experimentally measured LV data.

The SR-3 propeller test results obtained from the propeller test rig rotating balance and a flow survey probe are compared in Fig. 18 with the curved lifting line and the propeller/nacelle lifting line analytical codes. For consistency of comparison with experimental results, the analytical results account for the change in blade twist resulting from centrifugal forces generated by blade rotation. These data are presented over a range of advance ratios for a free-stream Mach number of 0.8. In the power coefficient curve, both analytical methods overpredict the power coefficient although the curved lifting line analysis more accurately predicts the level. Both methods deviate further from the data at both high and low advance ratios and are most accurate in the mid-range. The assumed variation of twist change with rotational speed affects the shape of the predicted power coefficient curve. The analysis prediction shown in Fig. 18 assumed that the twist varied with rotational speed squared and may be responsible for some of the discrepancy in the predicted and measured power coefficient results. For the efficiency curves, the curved lifting line analysis agrees well with the data while the propeller nacelle interaction analysis considerably underpredicts the efficiency at low advance ratios and considerably overpredicts the efficiency at high advance ratios. The differences between the results from the two methods appear to be primarily due to the different approaches used for obtaining lift.

Comparisons for radial distribution of loading are shown in Fig. 18(b) for the SR-3 propeller at a free-stream Mach number of 0.8 and an advance ratio of 3.06. The propeller nacelle interaction analysis more accurately predicts the loading distribution over most of the blade, deviating appreciably only in the outer 20 percent of the blade. The curved lifting line analysis overpredicts the loading inboard and underpredicts outboard, both by appreciable amounts.

A comparison of the analytical and experimental results recently obtained with the Euler lifting surface analysis can be seen in Figs. 19 to 21.

In Fig. 19, the predicted relative Mach number on the surface of the SR-3 propeller blades and between the blades is shown for the SR-3 propeller at a free stream Mach number of 0.8, an advance ratio of 3.06, and a blade angle of 61.3°. These data employ the same gray shading technique described for Fig. 17. The level of Mach numbers on the suction side of the blade near the nacelle surface at about the two-thirds chord indicates the presence of a shock wave at that location. On the pressure side of the blade, a shock wave is also indicated at about the same location. The middle portion of the figure shows the calculated Mach numbers between the blade passages near the hub and at 82 percent of the blade span. Near the hub, the shock wave is strong and spans the entire passage. At the 82 percent blade span location, the shock wave emanates from the suction surface near the trailing edge but becomes very weak near the pressure surface.

The results shown in Fig. 19 are in good qualitative agreement with laser velocimeter measurements presented in Ref. 26. One significant difference is the location of the shock wave. In the computed results, the shock wave originates closer to the trailing edge of the blade on the suction surface whereas the data of Ref. 26 indicates a shock wave location somewhat upstream of the trailing edge. This behavior is consistent with shock wave boundary layer interactions in other types of flow fields in which viscous effects cause the actual shock wave location to be upstream of the location predicted by inviscid analyses.

The Euler analysis results are next compared in Figs. 20 and 21 with experimentally measured propeller wake swirl angles and power coefficients at a free stream Mach numbers of 0.8. In Fig. 20, the Euler analysis values of swirl angle downstream of the propeller are compared with experimentally measured values of swirl angle obtained during the wind tunnel tests described in Ref. 9. These values were measured with an instrumented wedge mounted on a translating probe. Both the computed and measured values correspond to an axial location 0.21 propeller diameters downstream of the pitch change axis. Although the level of the predicted results is considerably higher than the experimental results, the radial variation of swirl is in reasonable agreement between the two sets of results. The swirl angle overprediction is approximately equal

to 4° whereas at a free stream Mach number of 0.6 (Ref. 15) the discrepancy was about 3°. Inasmuch as the Mach 0.6 discrepancy was presumed due to the lack of viscous effects in the analysis, the larger discrepancy at Mach 0.8 implies that a mechanism in addition to boundary layer growth is causing decreased flow turning. This mechanism could be due to the presence of the previously discussed shock wave located just upstream of the blade trailing edge. A shock wave boundary layer interaction resulting from this shock location would result in reduced blade loading and cause reduced swirl relative to a trailing edge shock wave location.

The compressor methodology of Ref. 29 was used to estimate the viscous losses at Mach 0.8 and a radius ratio of 0.52 where the solidity (chord/gap) is 1.0. The methodology is based on low speed cascade data and does not account for the presence or effects of shock waves. Because of shock losses, it was expected that the estimate of viscous effects would fall considerably short of the Euler analysis to data discrepancy. Surprisingly, the estimate falls only slightly short. The unusual behavior of the data near r/R = 1.0 was apparently caused by the tip vortex rollup. The analysis did not predict this feature of the flow because the mesh was too coarse in this region.

A comparison of the Euler computed and measured propeller power coefficients is shown in Fig. 21 for the SR-3 propeller at a Mach number of 0.8. Experimental results are taken from Ref. 9. The power coefficient (shown for three blade angle settings) was considerably overpredicted for each case shown. Since power coefficient is closely related to swirl angle, the over-prediction of power coefficient is consistent with the overprediction of swirl angle shown in Fig. 20.

PROPELLER ACOUSTIC RESEARCH

In order for an advanced turboprop aircraft to be competitive with an advanced turbofan aircraft, the turboprop fuselage interior should be equivalent in comfort (low levels of noise and vibration) to that of the turbofan aircraft. A quiet fuselage interior will be more difficult to achieve in the turboprop aircraft. This is because its fuselage may be in the direct noise field of the propeller whereas the inlet duct of a turbofan shields the fuselage from fan noise. In addition, the propeller tip vortex from a wing mounted tractor propeller induces significant wing surface pressure fluctuations that could be transmitted as structural borne noise to the fuselage interior (Ref. 30). Both of these areas are being investigated as part of the NASA propeller technology program; however, only the direct radiated noise will be covered in this paper. Advanced technologies are currently being evaluated to reducing propeller source noise and improving fuselage wall noise attenuation. Fuselage wall study results have shown improved wall attenuation potential with reduced weight penalty by using a double wall fuselage construction and lighter composite materials (Refs. 31 and 32). Reduced propeller source noise is being studied with propeller sweep and new acoustic analysis techniques.

The acoustic propeller analysis methods being used and under development by NASA are listed in Fig. 22 and include both steady and unsteady aerodynamic theory, along with several propagation models. The simplest acoustic code (A in Fig. 22) uses lifting line aerodynamics and two-dimensional airfoil data with the linear propagation theory of Farassat (Ref. 33). This analysis has been compared with propeller noise data and some results are presented later in this section of the paper. A more sophisticated analysis (B) developed and being used at Lewis is the three-dimensional nonlinear steady aerodynamics approach with linear time domain propagation (Ref. 34). This program uses the Denton code (Ref. 35) as adapted from a turbofan aerodynamics package and the Farassat time domain acoustic code for propagation from the steady loading and blade thickness sources. The above methods currently have only single rotation (SR) capability. The third analysis listed in Fig. 22 (C) is being developed under a Lewis grant to Texas A&M University. It will use the simpler lifting line analysis, two-dimensional airfoil data and the Farassat propagation theory to determine the steady loading effects of counter-rotating propellers. Unsteady aerodynamics need to be developed for this program to provide a more complete modeling of CR propeller flow fields.

A three-dimensional exact linear lifting surface theory is being developed under a Lewis contract to Hamilton Standard. A steady aerodynamics version will be developed first (D), followed by an unsteady version (G). The sound propagation model uses the linear frequency domain theory of Hanson (Ref. 36). The program will also contain an airframe flow theory which describes the installation effects of the fuselage, wing and nacelle. Boundary layer sound refraction effects on the fuselage (Ref. 37), and wing shielding of the noise propagation to the cabin are also planned to be included. A three-dimensional nonlinear steady aerodynamics method with a linear frequency domain sound propagation formulation (E) is under development in a Lewis contract program at General Electric. The aerodynamics are modified by a nonlinear Euler code (Refs. 18 and 19). This program will eventually include the installation effects on noise. Flow distortion resulting from airframe installation, as well as fuselage boundary layer and wing shielding effects are to be included in the program. Some initial unsteady aerodynamics capability (H) will also be added to this program by combining the aerodynamics of the actuator disk theory and the unloaded linear lift response theory.

A three-dimensional nonlinear steady aerodynamics approach (F) is being developed in a Lewis contracted program to Arvin/Calspan. This program will use the nonlinear Euler code to describe the near field and couple it to a linear integral analysis to extend the solution to the far field. The coupling is to be done on a cylindrical surface as in Ref. 38 and an iteration routine will provide the required matching of solutions

at the surface. This system will provide proper boundary conditions for the far field and allow nonlinear propagation effects in the near field.

Acoustic measurements have been made in the Lewis 8- by 6-Foot Wind Tunnel on several of the high-speed propeller models of Fig. 10. The noise data were obtained from pressure transducers located on the side-wall and ceiling of the tunnel. Acoustic results from tests of the SR-2, SR-1M, and SR-3 eight-bladed propellers are reported in Refs. 3 and 4, and results from tests of the SR-6 ten-bladed model are reported in Ref. 39. There were some initial concerns about the quality of the noise data obtained in this tunnel, however, the Refs. 3 and 4 results indicated that a relative comparison of noise levels measured in the tunnel for the various high-speed propellers would be valid.

The effect of blade sweep on propeller noise obtained from wind tunnel results is shown in Fig. 23. The maximum blade passage tone measured on the tunnel ceiling is plotted against the helical tip (total, including tunnel and rotational) Mach number. The data were obtained at approximately the design power coefficient by holding the advanced ratio constant. The helical tip Mach number was varied by changing tunnel and propeller rotational speed. In general, the noise of both swept and straight propellers increased rapidly as the helical tip speed approached Mach 1.0. At higher helical tip speeds the noise of all three propellers shown in Fig. 23 tended to level off. The aerodynamic sweep of the 30° swept propeller (SR-1M) produced a lower noise level than the straight propeller at the lower helical tip speeds. But this advantage decreased and eventually disappeared as the tip speed increased to Mach 1.2. The 45° sweep of the SR-3 propeller was tailored to provide additional noise reduction through increased sweep and acoustic phase cancellation. The success of this acoustic sweep design is evident from the data of Fig. 23. Over the complete test range, the noise level of the 45° swept propeller was consistently lower than that of the straight or 30° swept propeller, being 5 to 6 dB lower than the straight propeller at the design tip Mach number of 1.14 and 7 to 9 dB lower at the lowest tip speeds that were tested.

In addition to wind tunnel measurements, flight noise tests have been made using propeller models mounted above the fuselage of the Jetstar aircraft (Fig. 24). Comparisons of flight and wind tunnel noise data using the SR-3 propeller are reported in Refs. 40 and 41. The good agreement of these comparisons is currently being reexamined to insure that all potential sources of differences between the two tests are properly understood. Flight noise tests have also been conducted with the SR-2 and SR-6 propellers.

The simpler lifting line aerodynamics and the linear acoustic propagation theory as derived from some earlier work of Farassat (Refs. 42, 43, and 44) were used to predict the noise of the three initial propeller models (Fig. 9) and the results are reported in Ref. 45. A comparison of this theoretical prediction with tunnel data for the eight-bladed straight propeller (SR-2) is shown in Fig. 25. Generally good agreement is shown with the model data at tip speeds up to around Mach 1.0. Above a helical tip Mach number of 1.0, the theory overpredicts the near-field noise. The linear theory does not predict the levelling off of the peak noise as shown by the data. This levelling off of propeller noise at supersonic helical tip Mach numbers was observed in older propeller tests (Ref. 46). At these speeds, shock waves can propagate from a rotating propeller blade and cause nonlinear acoustic sources. To address this source, an initial simple shock wave noise model was formulated at the NASA Lewis Research Center (Ref. 47). This model predicts the noise resulting from the shock pressure rise caused by the propeller tip alone. The shock pressure rise prediction for the eight-bladed straight propeller is compared to the data in Fig. 25. Although the shock wave model predicts a rather substantial peak in the noise level not measured in the tunnel data, it also predicts the levelling-off trend in noise at the higher supersonic tip speeds that agrees with the trend in the tunnel data. This predicted trend indicates that the nonlinear shock wave model may be a viable method to pursue for enhancing the future acoustic modelling of high-speed propellers.

The effects of installation environments on propeller noise are also being investigated. Flow field distortion due to the influence of wings, nacelle, and fuselage can have an important influence upon the noise generated by a propeller. Recent experiments using an adjustable lifting wing and the SR-3 propeller have been conducted in the Lewis 8- by 6-Foot Wind Tunnel as shown in Fig. 26. Time variations in the pressure on the propeller blades due to the flow distortion have been measured using flush mounted pressure transducers. Preliminary results with the blade mounted pressure transducer data have been reported in Ref. 48. The major conclusions observed so far are that local oscillatory pressure cancellation occurs on the propeller blades due to interaction of the acoustic propagation and the unsteady aerodynamics and that the presence of the propeller significantly influences the flow-field distortion induced by the lifting wing.

Also seen in Fig. 26 is one of the four microphone mounting plates used to measure the unsymmetrical noise field produced by the unsteady loading of the propeller by the flow field. The noise data are now being analyzed and will be presented in the near future. The presence of the wing has been observed to significantly change the noise radiation from the propeller.

PROPELLER AEROELASTIC RESEARCH

Three major goals of advanced high speed propeller designs are to maximize aerodynamic efficiency, minimize noise and assure structural integrity. The acoustic and

aerodynamic requirements of high speed propellers have resulted in propellers with thin, highly swept and twisted blades of low aspect ratio and high solidity operating in transonic flow conditions. To assure the structural integrity of these advanced propellers, the NASA propeller technology program includes both experimental and analytical aeroelastic research that is applicable to the unconventional geometry and transonic flow conditions of these propellers and can be used to improve existing and develop new aeroelastic analyses. The aeroelastic research areas that are being investigated as a part of the high speed propeller program are shown in Fig. 27. These areas include the phenomena of stall flutter, forced-excitation and classical flutter. Stall flutter occurs at low flight speed conditions when the local blade angle-of-attack is high and separated flow occurs, whereas classical flutter involves unstalled flow and usually occurs at higher flight speeds. Forced excitations occur at both low and high flight speeds and can be due to cross-winds, upwash, airframe flow field distortions, and angled inflow with respect to the propeller thrust axis.

The aeroelastic propeller analysis methods that are currently being used and under development as part of the NASA program are listed in Fig. 28. Both structural blade models and unsteady aerodynamic models are shown. The swept straight-beam model (A in Fig. 28) is part of a classical flutter analysis that used two-dimensional subsonic and supersonic cascade (F), and two-dimensional transonic airfoil unsteady aerodynamics with sweep corrections (G). This analysis is based on a modification to the analysis described in Ref. 49. Some results from this analysis have been compared with propeller flutter data and are presented later in this section of the paper. A swept curved-beam model (B) is part of a more comprehensive aeroelastic analysis which is still in development under a NASA contract with United Technologies Research Center (Ref. 50). This analysis (which is based on a modification to an existing helicopter rotor code) has forced response, stall and classical flutter capabilities. The unsteady aerodynamics used for forced response and classical flutter are two-dimensional quasi-steady (D), subsonic airfoil with sweep correction (H), and empirical airfoil for stall flutter (E).

A plate finite element structural model (C) is part of a more sophisticated analysis developed under a contract with Bell Aerospace Textron and is being used at Lewis for classical flutter analysis (Ref. 51). This code is an extended version of the NASTRAN code modified for flutter analysis of turbomachinery, including turboprops and turbofans. This classical flutter analysis will be modified in the near future to include forced response analysis of advanced propellers. It uses the same unsteady aerodynmamics as the swept straight-beam classical flutter analysis (F and G). Some results from this code are also shown compared to experimental data later in this section.

An aeroelastic code being developed at Lewis will use the coupled normal modes and frequencies from a plate finite element structural program (C) and will include structural mistuning of blades. This code is planned to have forced response, stall and classical flutter capability. For classical flutter, the code will initially use the same unsteady aerodynamics as the swept straight-beam analysis (F and G). Later, a three-dimensional subsonic cascade unsteady aerodynamic code (I) which is being developed at Purdue University under a NASA grant will be substituted. Modified versions of the aerodynamic models from the swept curved-beam analysis will be used for stall flutter and forced response predictions.

Experimental aeroelastic research in progress at Lewis also includes work on forced excitation, stall flutter and classical flutter. Three of the high-speed propeller models are being used for this work: the eight-bladed unswept and 45° swept models (SR-2 and SR-3) and the ten-bladed 60° swept model (SR-5) (Fig. 10). These models, while having the same aeroacoustic characteristics and geometry as a large-scale design, are not, however, aeroelastically scaled. The experimental aeroelastic data that were obtained from them is, however, applicable to and is being used to help evaluate the accuracy of the aeroelastic analysis methods. Aeroelastic wind tunnel tests with the three models have been completed at freestream velocities from Mach 0 to 0.85 and at rotational speeds up to 9000 rpm. Stall flutter, classical flutter and forced response tests were done at NASA Lewis Research Center with an isolated nacelle model (Fig. 10) using all three propeller models. Also, a nacelle-wing-fuselage model (Fig. 29) was used at NASA Ames Research Center to obtain forced response data in a flowfield more representative of an aircraft installation. This was done with the eight-bladed unswept propeller model (SR-2). Similar tests are planned at Ames with the eight-bladed 45° swept model (SR-3).

The operating procedure used to conduct these experiments was to incrementally increase the propeller rotational speed, at a fixed blade pitch angle, thrust centerline pitch angle, and tunnel Mach number until a desired operating condition or limit was reached. The operating limits were blade stress, rotational speed, and rig power or vibration. The model was operated with the propeller thrust axis aligned with the freestream velocity for the flutter tests and at an angle-of-attack to the freestream velocity for the forced response tests. This angle-of-attack produced the aerodynamic excitation forces on the blades for the response study. Data were obtained from strain gauges installed on the surface of selected blades.

Some results from the propeller forced excitation tests at 0.8 Mach number are shown in Fig. 30. Comparisons between measured and predicted one-P vibratory blade stress are shown from the isolated nacelle tests for the eight-bladed unswept and 45° swept models and the ten-bladed 60° swept model. A comparison from the installed test (Fig. 29) is shown for the eight-bladed unswept model. The data presented were obtained

by an inboard uniaxial strain gauge and its location for the 45° swept blade is shown in the figure. For the isolated nacelle case shown in Fig. 30, the predicted value of one-P stress agreed well with the data for the unswept propeller but showed only reasonable agreement with the swept propeller data and tended to underpredict their measured stress levels. For the installed case, there were two analysis methods used. Both tended to overpredict the measured stress level.

The predicted values used in Fig. 30 were calculated by Hamilton Standard under contract to NASA Lewis using company developed codes that incorporated two-dimensional quasi-steady aerodynamics. The aerodynamics were combined with a beam analysis for the unswept propeller and a finite element analysis for the swept propeller models. Two different flow field calculations were used for the installed analysis. The first was the Douglas-Neumann Potential Flow Program (Ref. 52) which is a lifting surface method. It produced the stress ratio of 0.8 shown in Fig. 30. The second was a Hamilton Standard inhouse program that represented the fuselage by a Rankine solid and the wing by a lifting line. This method produced the lower stress ratio of 0.4 in Fig. 30. These results indicate that the more accurate flow field calculation of the lifting surface method resulted in a better prediction capability at Mach 0.8. However, at lower Mach numbers, the two methods produced more comparable results.

During high speed wind tunnel tests a classical coupled bending-torsion flutter phenomena was encountered with the ten-bladed 60° swept propeller model, SR-5 (Ref. 53). The other two propeller models experienced no flutter. The flutter was encountered over the tested Mach number range of 0.6 to 0.85 and occurred when the blade helical tip Mach number reached a value of about 1.0 over a range of blade angles and power loadings. A theoretical study made after this flutter experience suggested that sweep and aerodynamic cascade effects have a strong destabilizing influence on the flutter boundary. The theoretically predicted destabilizing effect of sweep on flutter was experimentally supported by the fact that only the most highly swept of the three tested propellers encountered flutter. To experimentally investigate the aerodynamic cascade effect, a five- and two-bladed configuration of the SR-5 model was subsequently tested. This experiment supported the theoretical predictions by showing that the flutter onset occurred at a lower helical tip Mach number when there were a larger number of blades on the rotor. These results are illustrated in Fig. 31 which shows the experimental flutter boundary for the ten- and five-bladed configurations at a selected blade angle of 69°. The flutter boundary data are shown in terms of the flutter onset rotational speed versus free-stream Mach number. Also shown are two theoretical predictions for the flutter boundary of the ten-bladed configuration. These boundaries were predicted by the swept straight-beam and the plate finite element classical flutter aeroelastic analysis codes that were described earlier in this section. Both of these analyses and the experimental data of Fig. 31 show the same trend of decreasing flutter rotational speed with increasing free-stream Mach number. Although the slopes of the experimental and calculated boundaries are different they are in reasonable agreement. However, the figure shows that both of the predicted boundaries are conservative, and increasingly underpredict the experimental boundary as the Mach number increases.

Future efforts in aeroelastics will be directed toward improving the existing analysis codes and developing new aeroelastic codes with better prediction capabilities and accuracy. Experimental to analytical comparisons will continue to be a primary tool to identify areas where the codes need improving. Future experimental work will include a model of the eight-bladed 45° swept propeller fabricated from composite materials (SR-3C). This model will soon undergo isolated forced response and flutter testing in the Lewis 8- by 6-Foot Wind Tunnel. Installed forced response testing in the Ames 14-ft tunnel is also planned for this model. These efforts will be followed by the testing of a new high-speed propeller model (SR-7) that is aeroelastically scaled from a 9-ft propeller design.

FUTURE TRENDS

The NASA advanced high-speed propeller research program has been primarily directed toward developing technology for high performing single-rotation (SR) tractor propellers. The performance results achieved with SR propeller models show that future advanced turboprop powered aircraft should be potentially far superior in performance to an equivalent turbofan powered aircraft. Wind tunnel model results have shown propeller efficiencies near 80 percent at Mach 0.8 with near-field cruise noise reductions with swept blades of about 6 dB. Further efficiency improvements and noise reductions may be possible with some of the advanced experimental and analytical technology work that is underway or planned as part of this research program. Two additional SR propeller models are currently being designed to address the speed range from Mach 0.7 to 0.8. The latest refinements to the evolving advanced analysis methods in aerodynamics, acoustics, and aeroelastics are being used to assist in the design of these models.

A number of attractive advanced turboprop concepts (Fig. 32) are being studied to further improve performance and reduce propeller noise. A single-rotation pusher propeller mounted at the rear of the aircraft fuselage (away from the cabin section) could reduce or possibly eliminate the potentially high cabin noise associated with a tractor wing-mounted configuration without incurring a weight penalty for cabin wall acoustic treatment. Advanced concepts that have the potential for recovering the residual swirl loss from SR turboprops could offer large improvements in propeller efficiency. Variable pitch stators behind a single-rotation propeller is one concept that offers increased efficiency through swirl recovery. Although the potential performance gains are not predicted to be as large as those for counter-rotation (CR) propellers, the stator

concept has the advantage of minimum complexity. However, the more complex CR propellers have the potential for recovering essentially all of the swirl losses. Advanced CR concepts that are being investigated as part of the NASA program include both pusher and tractor designs. One particularly unique pusher design is a gearless concept being investigated as part of a NASA contract program with General Electric. This concept eliminates the gearbox altogether but introduces the new concept of an integral counter-rotating power turbine.

The potential advantages of CR propellers over SR propellers is shown in Fig. 33 where ideal efficiency (optimum loading with zero blade drag) is plotted versus power loading for propellers operating at a typical Mach 0.8 cruise condition. The figure shows that performance gains by increasing blade count from 8 to 10 with SR propellers are rather small (about 1 percent) compared to the gains achievable by selecting CR over SR systems. At power loadings from 200 to 320 kW/m^2 (25 to 40 hp/ft^2) the CR potential efficiency gains range from about 6 to 9 percent for equal total blade count. As power loading is further increased, the SR propellers suffer a larger performance loss compared to CR systems due primarily to increasing swirl losses. Therefore, CR propellers can be operated at much higher power loadings (with associated propeller diameter and weight reductions) than SR systems without large performance losses. In addition, CR propellers with total blade counts comparable to SR propellers should also reduce potential blade-to-blade choking losses incurred in the inboard region of the 8 to 10 blade SR propellers by providing a larger flow area between the blades.

A recent NASA sponsored study that compared SR and CR geared tractor turboprops for a Mach 0.8 commercial transport application is reported in Refs. 2 and 54. This study focused on evaluating a number of propeller and gearbox concepts on a 100-passenger, twin engine airplane with a 1300 nmi design mission. The concepts with the most attractive operating costs were an advanced six by six-bladed CR propeller with an in-line differential planetary gearbox and an advanced ten-bladed SR propeller with an offset compound idler gearbox.

The study results are summarized in Fig. 34. The advanced CR propeller system was projected to have an 8 percentage point higher efficiency due to swirl recovery and a higher blade count, with only a 17 percent increase in propeller weight and 1.6 dBA cruise interior noise increase. The compact one-stage differential planetary gearbox would be 15 percent lighter and have a 0.2 percent higher efficiency than the gearbox system required for SR turboprops. There did appear to be an increase in acquisition cost of 19 percent with the CR gearbox. However, CR propeller systems offered an almost complete (-80 to -100 percent) cancellation of aircraft torque and gyroscopic loads. Because of the slightly higher CR propeller interior noise (1.6 dBA) and lower frequency noise content, the cabin acoustic treatment weight would have to be increased by about 5 percent. Based on these performance and weight changes, a 9 percent block fuel savings and a 2.9 percent DOC reduction was estimated for an advanced CR system relative to a comparable SR system for the 1300 nmi design mission.

To verify the performance gains projected for advanced CR turboprops, NASA has planned and recently initiated an extensive CR wind tunnel program. The program includes the testing of several 0.62 m (two ft) diameter model propellers that include both tractor and pusher configurations. Figure 35 is a photograph of a 16-bladed CR model of a gearless pusher configuration installed on a 1119 kW (1500 hp) propeller test rig.

REFERENCES

1. Jeracki, R. J., Mikkelson, D. C., and Blaha, B. J., "Wind Tunnel Performance of Four Energy Efficient Propellers Designed for Mach 0.8 Cruise," SAE Paper 790573, 1979.
2. Weisbrich, A. L., Godston, J. and Bradley, E., "Technology and Benefits of Aircraft Counter Rotation Propellers," (HSER-8858, Hamilton Standard; NASA Contract NAS3-23043.) NASA CR-168258, 1982.
3. Dittmar, J. H., Blaha, B. J., and Jeracki, R. J., "Tone Noise of Three Supersonic Helical Tip Speed Propellers in a Wind Tunnel at 0.8 Mach Number," NASA TM-79046, 1978.
4. Dittmar, J. H. Jeracki, R. J. and Blaha, B. J., "Tone Noise of Three Supersonic Helical Tip Speed Propellers in a Wind Tunnel," NASA TM-79167, 1979.
5. Mikkelson, D. C., Blaha, B. J., Mitchell, G. A., and Wikete, J. E., "Design and Performance of Energy Efficient Propellers for Mach 0.8 Cruise," SAE Paper 770458, 1977.
6. Hanson, D. B., "Near Field Noise of High Tip Speed Propellers in Forward Flight," AIAA Paper 76-565, 1976.
7. Metzger, F. B., and Rohrbach, C., "Aeroacoustic Design of the Prop-Fan," AIAA Paper 79-0610, 1979.
8. Bober, L. J., and Mitchell, G. A., "Summary of Advanced Methods for Predicting High Speed Propeller Performance," AIAA Paper 80-0225, 1980.
9. Rohrbach, C., Metzger, F. B., Black, D. M., and Ladden, R. M., "Evaluation of Wind Tunnel Performance Testings of an Advanced 45° Swept Eight-Bladed Propeller at Mach Numbers from 0.45 to 0.85," NASA CR-3505, 1982.
10. Dugan, J. F., Jr., Gatzen, B. S., and Adamson, W. M., "Prop-Fan Propulsion - Its Status and Potential," SAE Paper 780995, 1978.
11. Swallow, R. J., and Aiello, R. A., "NASA Lewis 8- by 6-Foot Supersonic Wind Tunnel," NASA TM X-71542, 1974.

12. Mikkelson, D. C., and Mitchell, G. A., "High Speed Turboprops for Executive Aircraft, Potential and Recent Test Results," NASA TM-81482, 1980.
13. Jeracki, R. J., and Mitchell, G. A., "Low and High Speed Propellers for General Aviation - Performance Potential and Recent Wind Tunnel Test Results," NASA TM-81745, 1981.
14. Mitchell, G. A. and Mikkelson, D. C., "Summary and Recent Results from the NASA Advanced High-Speed Propeller Research Program," AIAA Paper 82-1119, 1982.
15. Stefko, G. L., Bober, L. J. and Neumann, H. E., "New Test Techniques and Analytical Procedures for Understanding the Behavior of Advanced Propellers," NASA TM-83360, 1983.
16. Goldstein, S., "On the Vortex Theory of Screw Propellers," Royal Society (London) Proceedings, Vol. 123, Series A, No. 792, 1929, pp. 440-465.
17. Chaussee, D. S., "Computation of Three-Dimensional Flow Through Prop Fans," NEAR TR-199, Nielsen Engineering and Research, Inc., 1979.
18. L. J. Bober, D. S. Chaussee and P. Kutler, "Prediction of High Speed Propeller Flow Fields Using a Three-Dimensional Euler Analysis," AIAA Paper 83-0188, 1983.
19. D. S. Chaussee and P. Kutler, "User's Manual for Three-Dimensional Analysis of Propeller Flow Fields," (FSI-80-04, Flow Simulations, Inc.; NASA Contract NAS3-22375.) NASA CR-167959, 1983.
20. Sullivan, J. P., "The Effect of Blade Sweep on Propeller Performance," AIAA Paper 77-716, 1977.
21. Egolf, T. A., Anderson, O. L., Edwards, D. E., and Landgrebe, A. J., "An Analysis for High Speed Propeller-Nacelle Aerodynamic Performance Prediction; Volume 1, Theory and Initial Application and Volume 2, User's Manual for the Computer Program," R79-912949-19, United Technologies Research Center, 1979.
22. W. H. Jou, "Finite Volume Calculations of Three-Dimensional Flow Around a Propeller," AIAA Paper 82-0957, 1982.
23. Bober, L. T., and Chang, L. K., "Factors Influencing the Predicted Performance of Advanced Propeller Designs," NASA TM-82676, 1981.
24. Serafini, J. S., Sullivan, J. R., and Neumann, H. E., "Laser-Velocimeter Flow-field Measurements of an Advanced Turboprop," AIAA Paper 81-1568, 1981.
25. R. J. Freedman and J. P. Greissing, "The Development and Utilization of a Laser Velocimeter System for a Large Transonic Wind Tunnel," NASA TM-82886, 1982.
26. H. E. Neumann, L. J. Bober, J. S. Serafini and L. K. Chang, "An Analytical and Experimental Comparison of the Flow Field of an Advanced Swept Turboprop," AIAA Paper No. 83-0189, 1983.
27. B. H. Anderson, C. W. Putt and C. C. Giamati, "Application of Computer Generated Color Graphic Techniques to the Processing and Display of Three Dimensional Fluid Dynamic Data," NASA TM-82658, 1981.
28. B. H. Anderson, C. W. Putt and C. C. Giamati, "Fluid Dynamic Data in Color and Three Dimensions," Mechanical Engineering, Vol. 104, No. 3, 1982, pp. 30-35.
29. I. A. Johnsen and R. O. Bullock, Editors, "Aerodyanmic Design of Axial-Flow Compressors," NASA SP-36, 1965.
30. Miller, B. A., Dittmar, J. H., and Jeracki, R. J., "The Propeller Tip Vortex - A Possible Contributor to Aircraft Cabin Noise," NASA TM-81768, 1981.
31. Revell, J. D., Balena, F. J., and Koval, L. R., "Analytical Study of Interior Noise Control by Fuselage Design Techniques on High-Speed, Propeller-Driven Aircraft," (LR-29382, Lockheed-California Co.; (NASA Contract NAS1-15427.) NASA CR-159222, 1980.
32. Rennison, D. C., Wilby, J. F., and Marsh, A. H., "Interior Noise Control Prediction Study for High-Speed Propeller-Driven Aircraft," (BBN-4026, Bolt, Beranek, and Newman, Inc.; NASA Contract NAS1-15426.) NASA CR-159200, 1979.
33. Martin, R. M., and Farassat, F., "User's Manual for a Computer Program to Calculate Discrete Frequency Noise of Conventional and Advanced Propellers," NASA TM-83135, 1981.
34. Clark, B. J., and Scott, J. R., "Coupled Aerodynamic and Acoustic Predictions for Turboprops," presented at the 107th Meeting of the Acoustical Society of America, 6-10 May, 1984, Norfolk, Va.
35. Denton, J. D., and Singh, U. K., "Time Marching Methods for Turbomachinery Flow Calculation," in Application of Numerical Methods to Flow Calculations in Turbomachines, von Karman Institute for Fluid Dynamics Lecture Series 1979-7, von Karman Institute for Fluid Dynamics, 1979.
36. Hanson, D. B., "Compressible Helicoidal Surface Theory for Propeller Aerodynamics and Noise," AIAA Journal, Vol. 21, No. 6, 1983, pp. 881-889.
37. Hanson, D. B., and Magliozzi, B., "Propagation of Propeller Tone Noise Through a Fuselage Boundary Layer," AIAA Paper 84-0248, 1984.
38. Hawkings, D., "Noise Generation by Transonic Open Rotors," Research Paper 599, Westland Helicopters Limited, 1979.
39. Dittmar, J. H., Stefko, G. L., and Jeracki, R. J., "Noise of the 10-Bladed, 40° Swept SR-6 Propeller in a Wind Tunnel," NASA TM-82950, 1982.
40. Dittmar, J. H., and Lasagna, P. L., "A Preliminary Comparison Between the SR-3 Propeller Noise in Flight and in a Wind Tunnel," NASA TM-82805, 1982.
41. Mackall, K. G., Lasagna, P. L., and Dittmar, J. H., "In-Flight Acoustic Results from an Advanced Design Propeller at Mach Numbers Up to 0.8," AIAA Paper 82-1120, 1982.
42. Farassat, F., "Theory of Noise Generation from Moving Bodies with an Application to Helicopter Rotors," NASA TR R-451, 1975.
43. Farassat, F., "Discontinuities in Aerodynamics and Aeroacoustics - The Concept and Applications of Generalized Derivatives," Journal of Sound and Vibration, vol. 55, no. 2, 1977, pp. 165-193.

44. Farassat, F., Morris, C. E. K., and Nystrom, P. A., "A Comparison of Linear Acoustic Theory with Experimental Noise Data for a Small Scale Hovering Rotor," AIAA Paper 79-0609, 1979.
45. Dittmar, J. H., "A Comparison Between the Existing Propeller Noise Theory and Wind Tunnel Data," NASA TM-81519, 1980.
46. Hubbard, H. H., and Lassiter, L. W., "Sound From a Two-Blade Propeller at Supersonic Tip Speeds, NACA Rep. 1079, 1952.
47. Dittmar, J. H., and Rice, E. J., "A Shock Wave Approach to the Noise of Supersonic Propellers," NASA TM-82752, 1981.
48. Heidelberg, L. J., Dahl, M. D., and Rice, E. J., "Measurements of Periodic Blade Pressures on a Transonic Propeller with Nonuniform Inflow," presented at the 107th Meeting of the Acoustical Society of America, 6-10 May, 1974, Norfolk, Va.
49. Kaza, K. R. V. and Kielb, R. E., "Coupled Bending-Bending-Torsion Flutter of a Mistuned Cascade With Nonuniform Blades," NASA TM-82813, 1982.
50. Bielawa, R. L., Johnson, S. A., Chi, R. M. and Gangwani, S. T., "Aeroelastic Analysis for Propellers - Mathematical Formulations and Program User's Manual," NASA CR-3729, 1983.
51. Elchuri, V., and Smith, G. C. C., "Flutter Analysis of Advanced Turboprop Propellers," AIAA Paper 83-0846, 1983.
52. Hess, J. L., "Calculation of Potential Flow About Arbitrary Three-Dimensional Lifting Bodies," Report MDC-J5679-01, Douglas Aircraft Co., Inc., Oct. 1972.
53. Mehmed, O., Kaza, K. R. V., Lubomski, J. F., and Kielb, R. E., "Bending-Torsion Flutter of a Highly Swept Advanced Turboprop," NASA TM-82975, 1982.
54. Strack, W. C., Knip, G., Weisbrich, A. L., Godson, J., and Bradley, E., "Technology and Benefits of Aircraft Counter Rotation Propellers," NASA TM-82983, 1982.

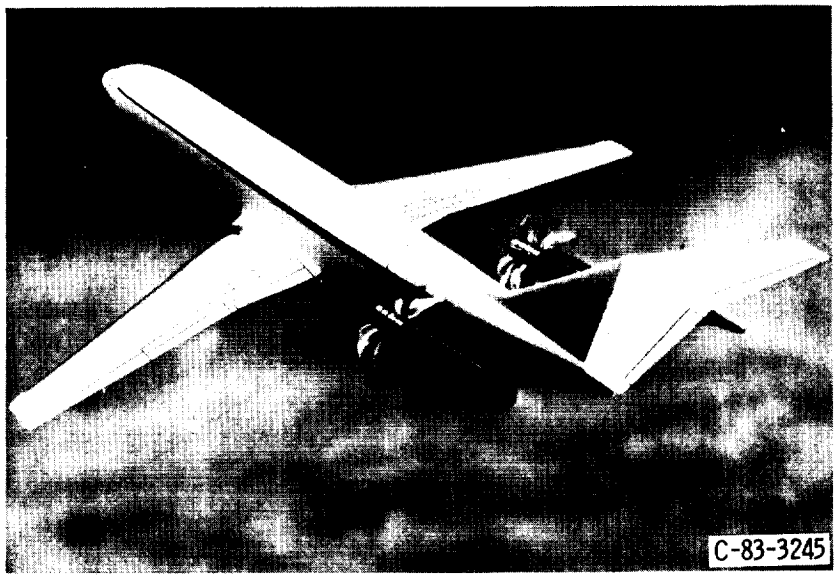

Figure 1. - Advanced counter-rotation turboprop aircraft.

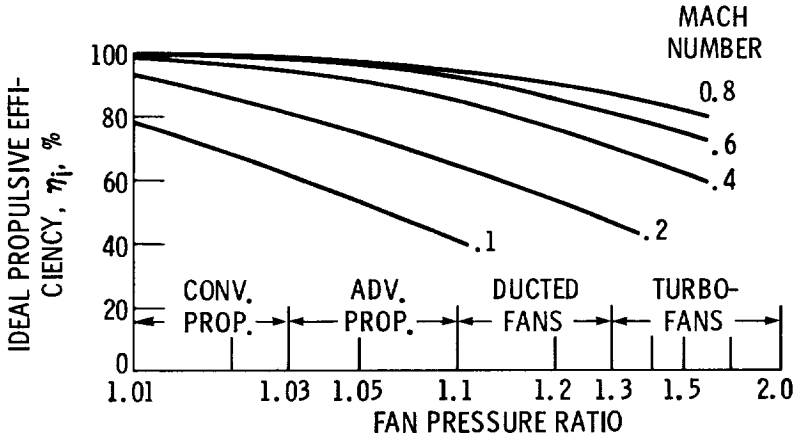

Figure 2. - Ideal propulsive efficiency as a function of fan pressure ratio.

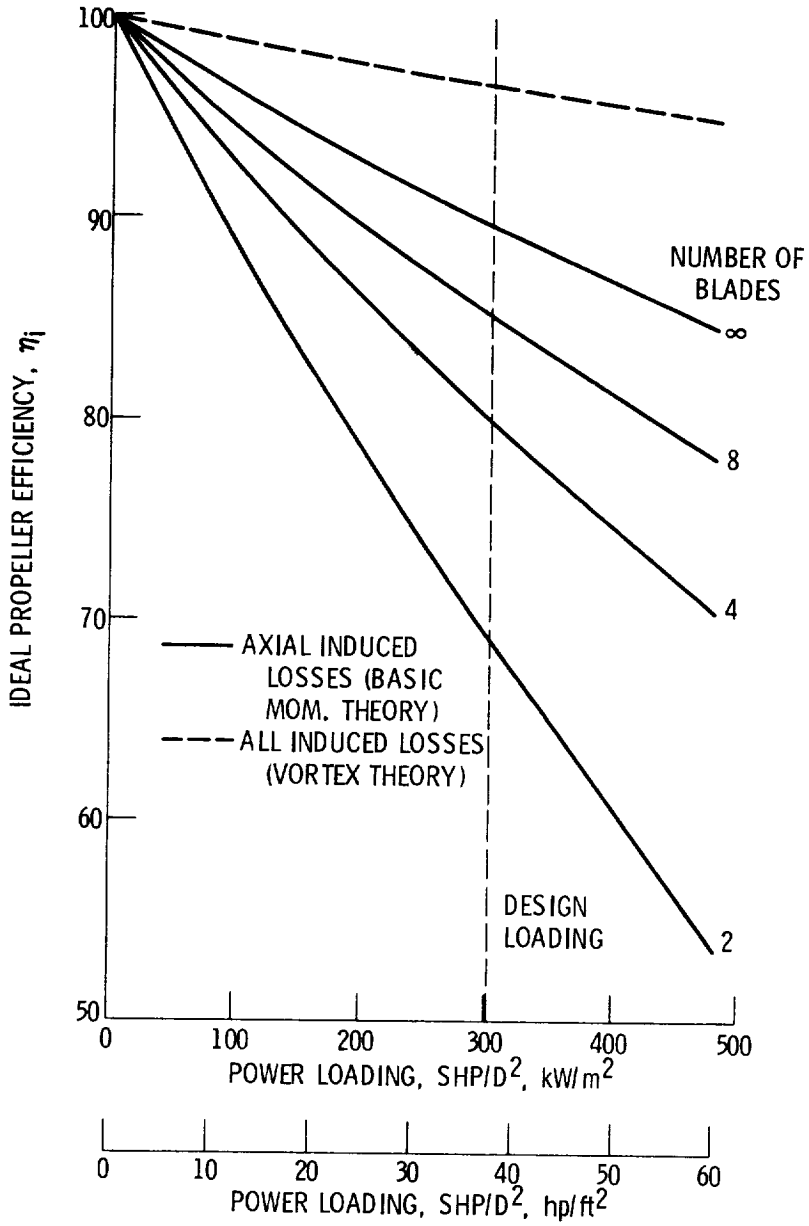

Figure 3. - Ideal single-rotation propeller efficiency; 0.8 Mach number at 10.668 km (35 000 ft) altitude and 243.8 m/sec (800 ft/sec) tip speed.

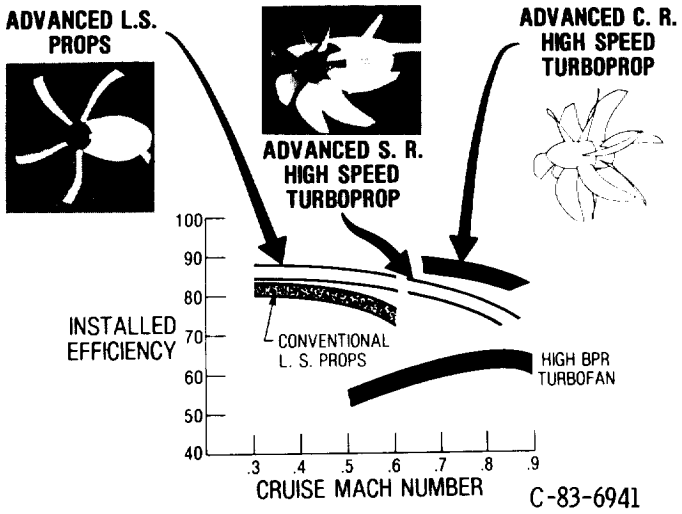

Figure 4. - Installed cruise efficiency trends.

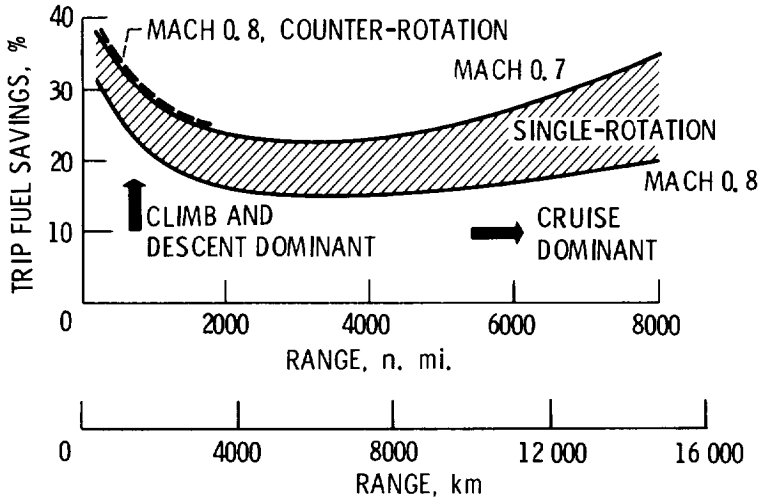

Figure 5. - Fuel savings trends of advanced turboprop aircraft over comparable turbofan aircraft.

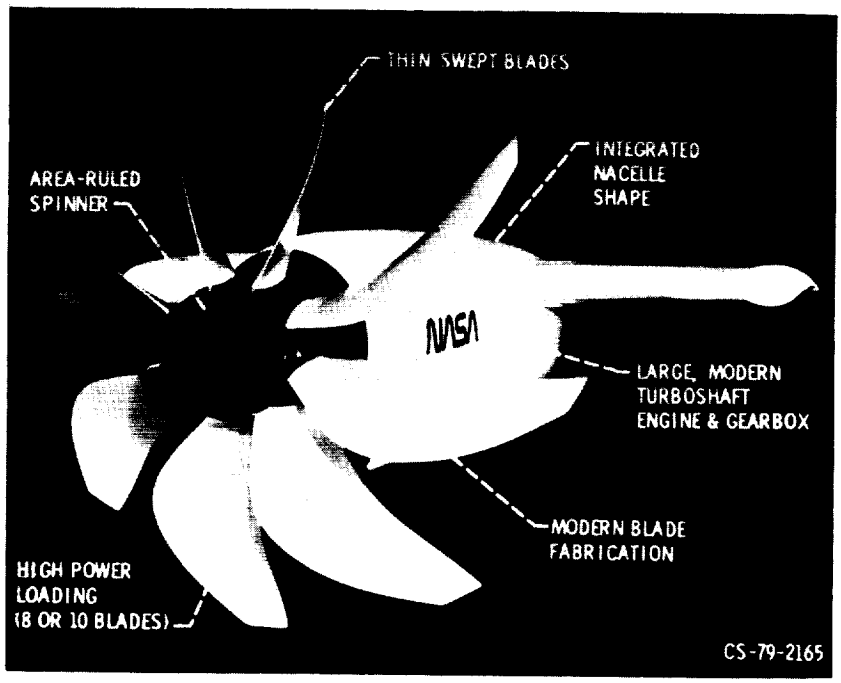

Figure 6. - Advanced turboprop propulsion system.

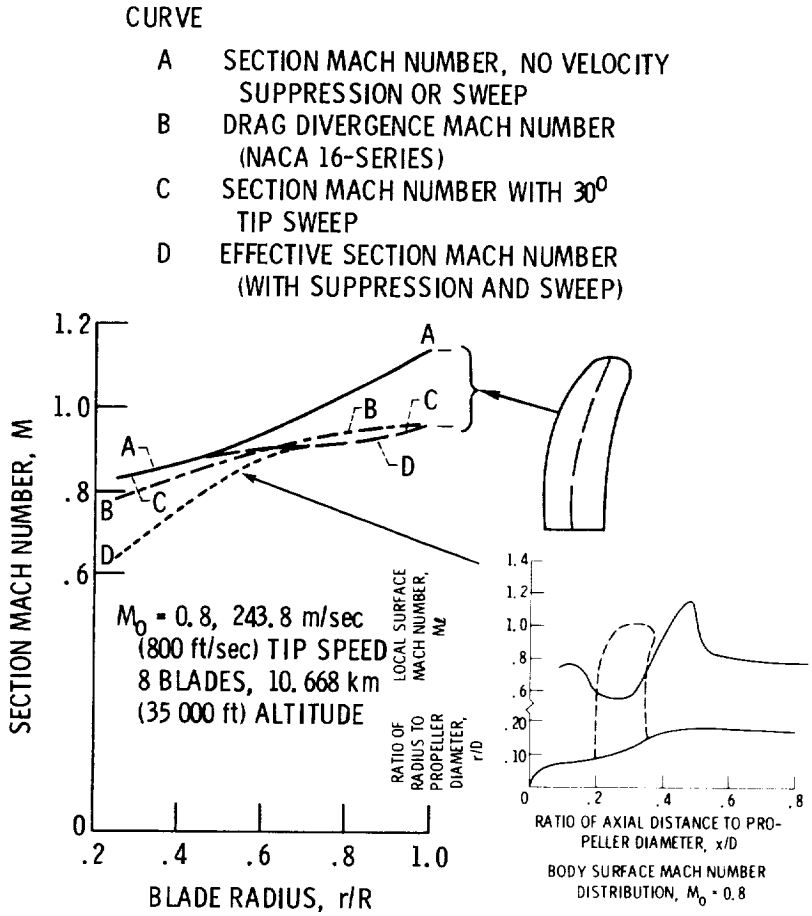

Figure 7. - Effects of advanced aerodynamic concepts on blade section Mach number distributions.

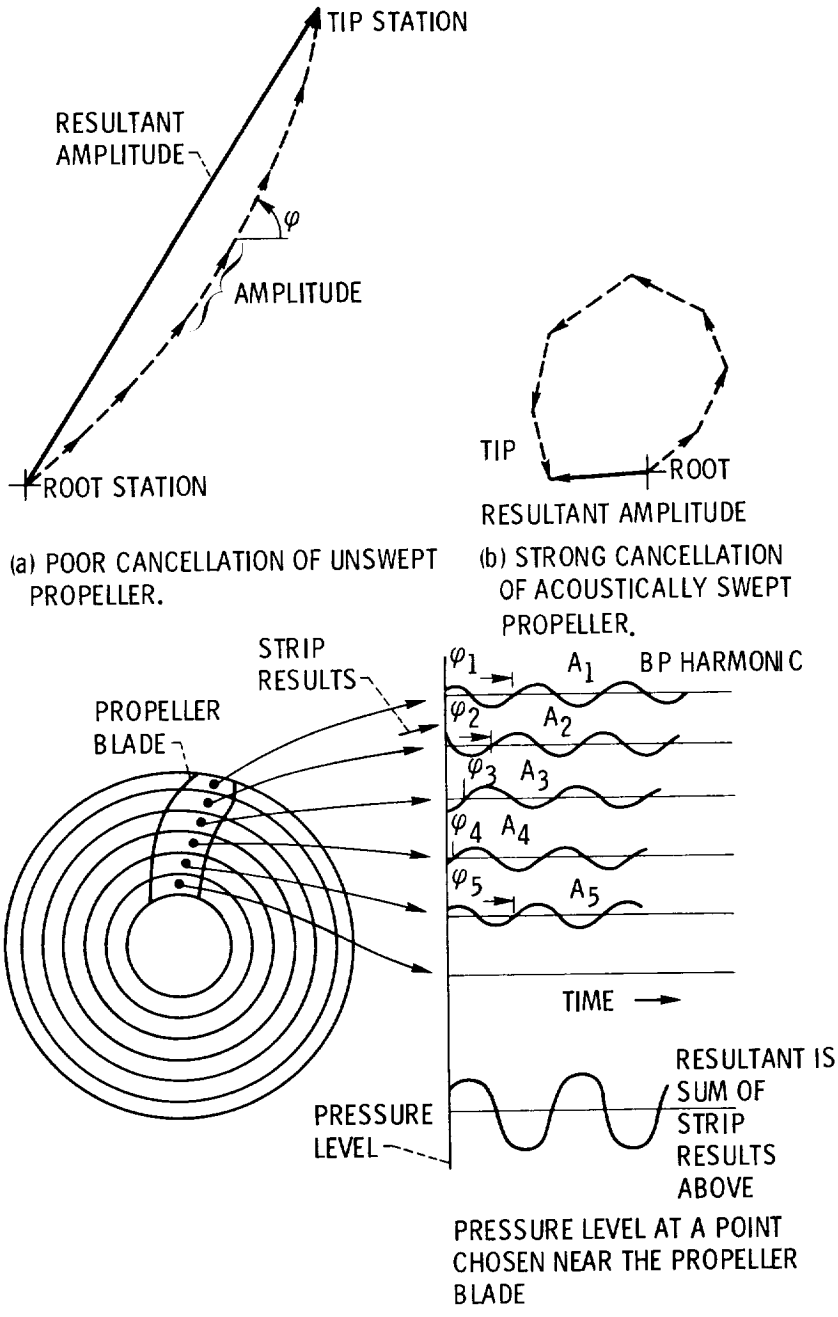

Figure 8. - Acoustic strip analysis technique for near-field noise reduction.

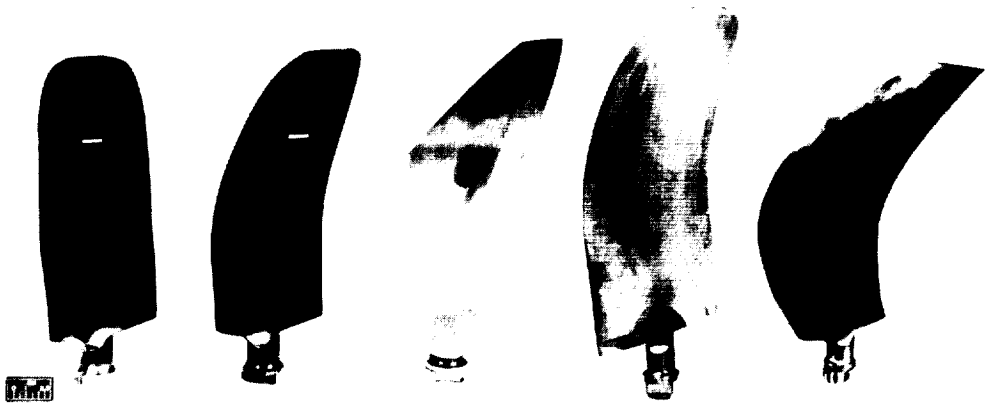

	SR-2	SR-1M	SR-3	SR-6	SR-5
TIP SWEEP ANGLE, deg	0	30	45	40	60
PREDICTED DESIGN NOISE REDUCTION, ΔdB	REF.	-3	-6	-6	-14
TIP SPEED, ft/sec (m/sec)	800 (244)	→	→	700 (213)	600 (183)
POWER LOADING, SHP/D^2 hp/ft^2 (kW/m^2)	37.5 (301)	→	→	30.0 (241)	26.0 (209)
NO. OF BLADES	8	→	→	10	10

Figure 9. - Design characteristics and planforms of high speed propeller models.

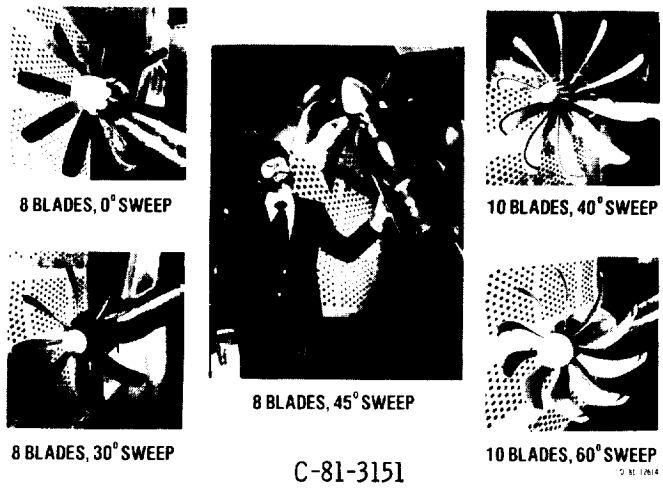

Figure 10. - Propeller models installed in the Lewis 8-by-6 foot wind tunnel.

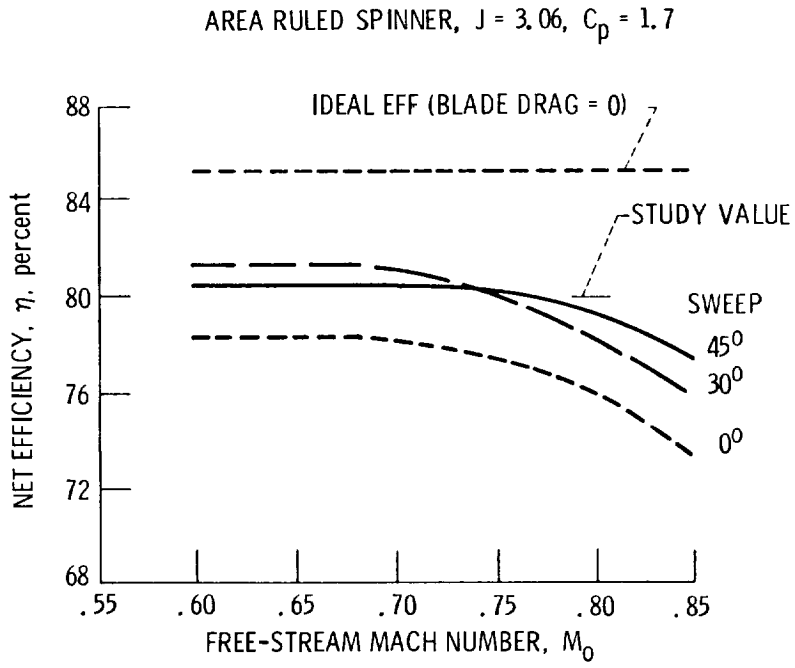

Figure 11. - Performance summary of 8-bladed propellers.

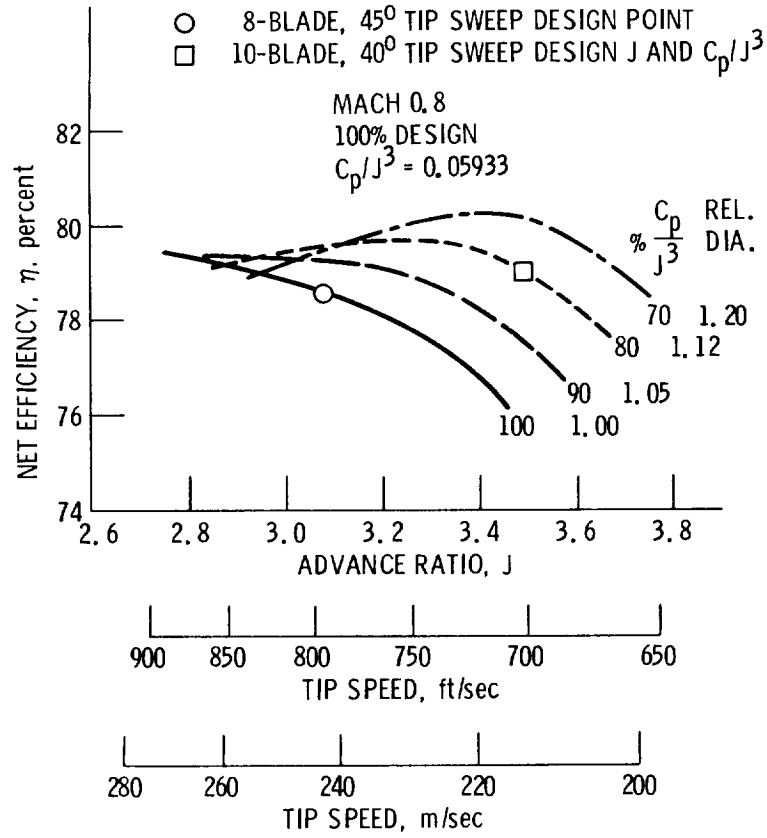

Figure 12. - Effect of power loading and advance ratio on performance of the 8-bladed 45° swept propeller (SR-3).

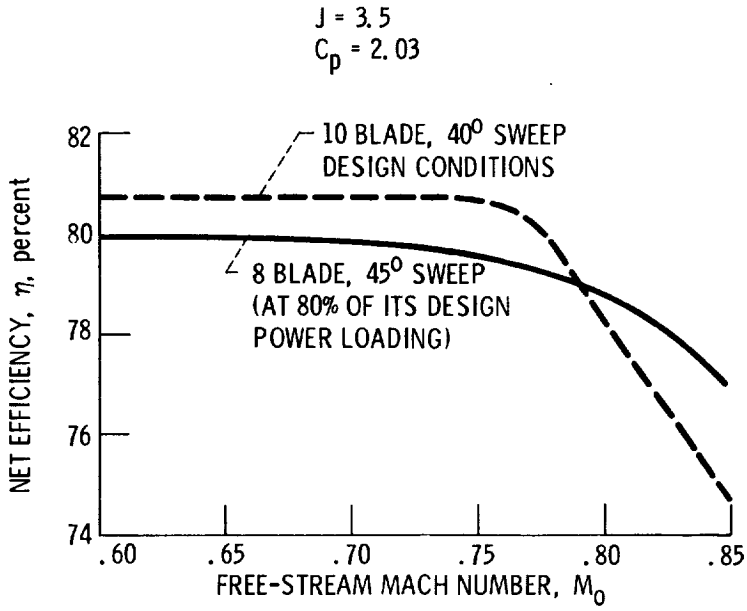

Figure 13. - Comparison of 8 and 10 blade performance.

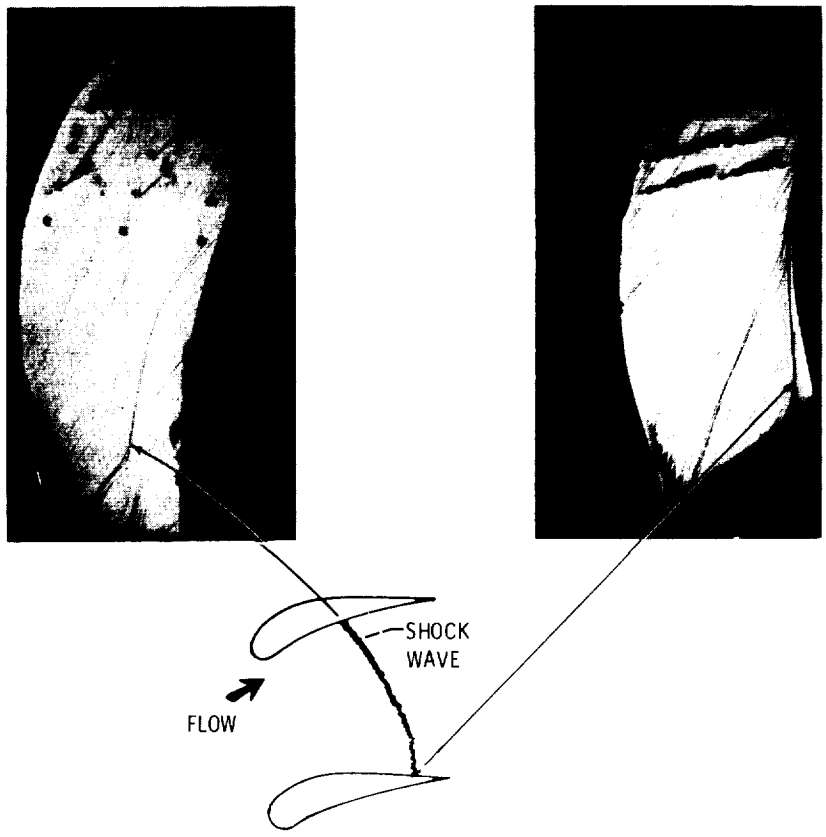

Figure 14. - Results from the paint flow visualization technique indicating the interblade shock structure on the 10-bladed, 40° swept propeller at Mach 0.8.

LIFTING LINE ANALYSES

STRIP ANALYSIS -SR
CURVED LIFTING LINE -SR, CR
PROPELLER/NACELLE -SR, CR

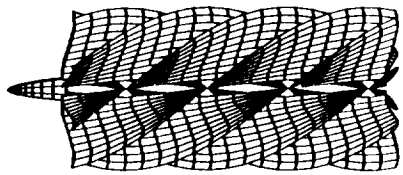

LIFTING SURFACE ANALYSES

TRANSONIC POTENTIAL -SR
EULER EQUATIONS -SR, CR
NAVIER-STOKES -SR

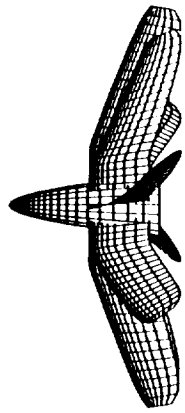

Figure 15. - Advanced analysis methods for improving propeller performance.

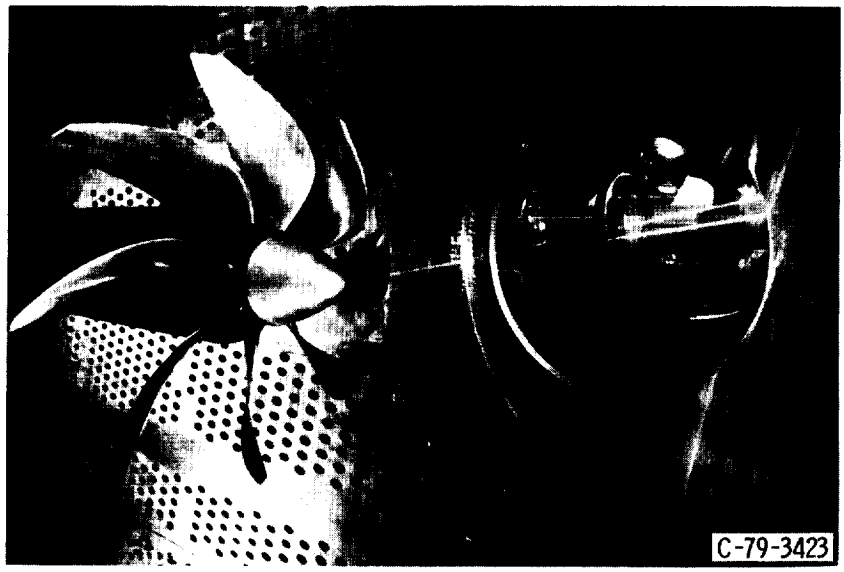

Figure 16. - Laser velocimeter in Lewis 8-by-6 foot wind tunnel.

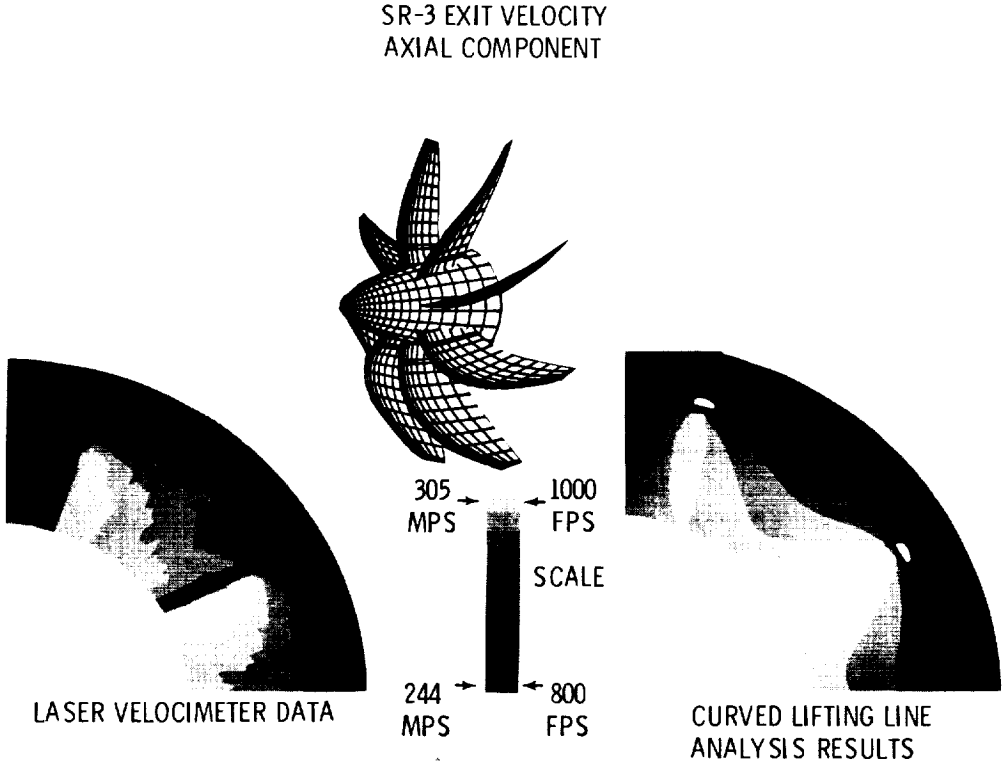

Figure 17. - Axial exit velocity comparisons between laser velocimeter data and curved lifting line analysis on the SR-3 propeller at Mach 0.80.

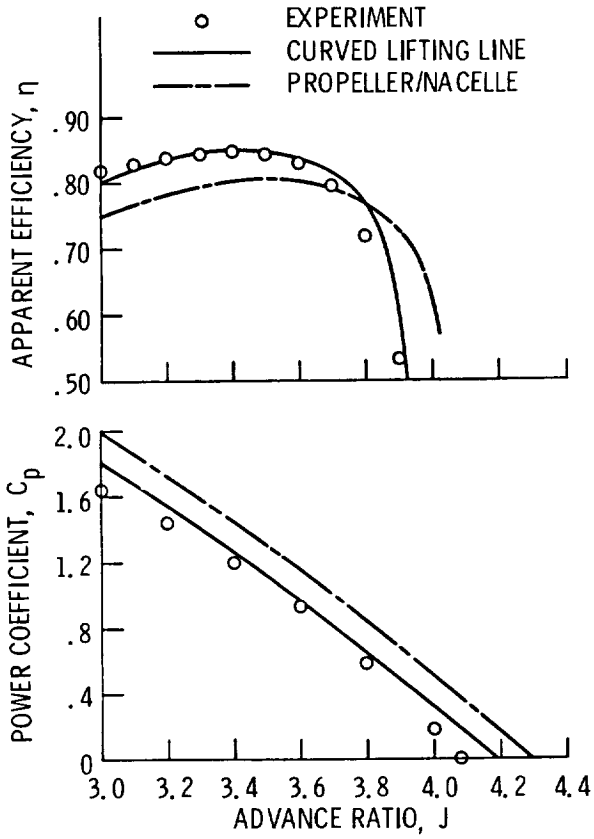

(a) Propeller performance. Blade angle at 3/4 radius equals 60.4°.

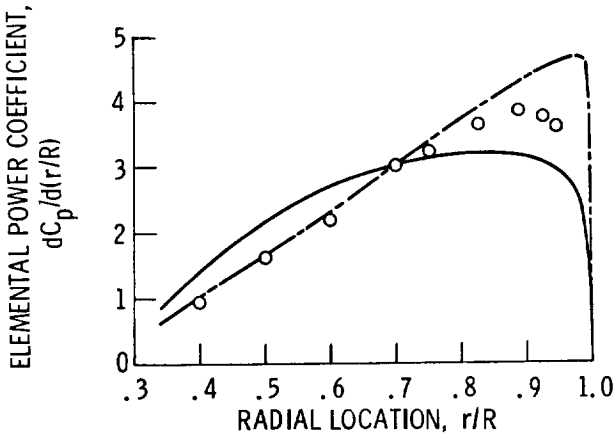

(b) Power loading distribution. Advance ratio equals 3.06.

Figure 18. - Comparison of lifting line analytical and experimental results for the SR-3 propeller at free stream Mach number of 0.8.

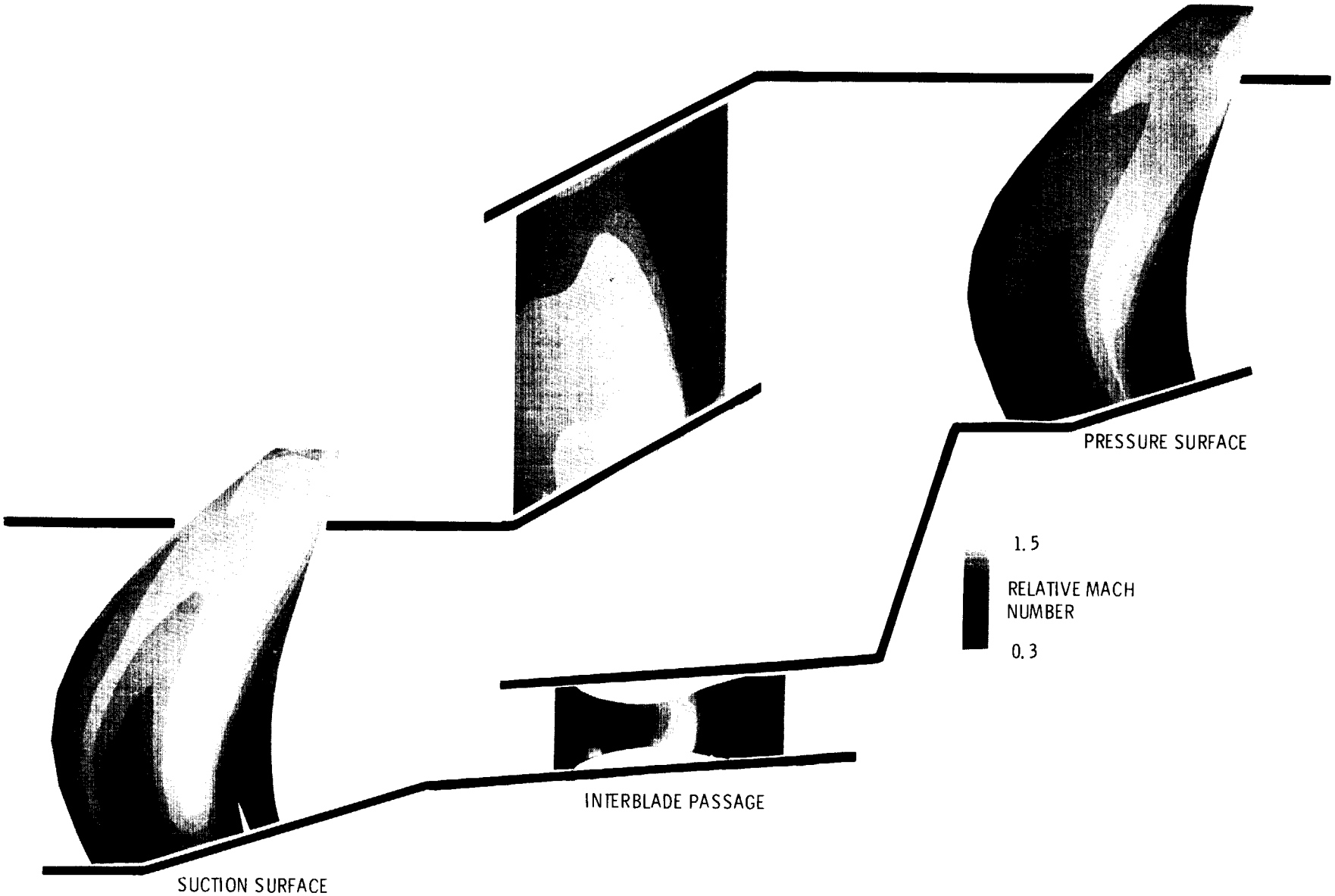

Figure 19. - Euler lifting surface analysis Mach number contours. SR-3 propeller at Mach 0.80, advance ratio 3.06, and blade angle at three-quarter radius 61.3.

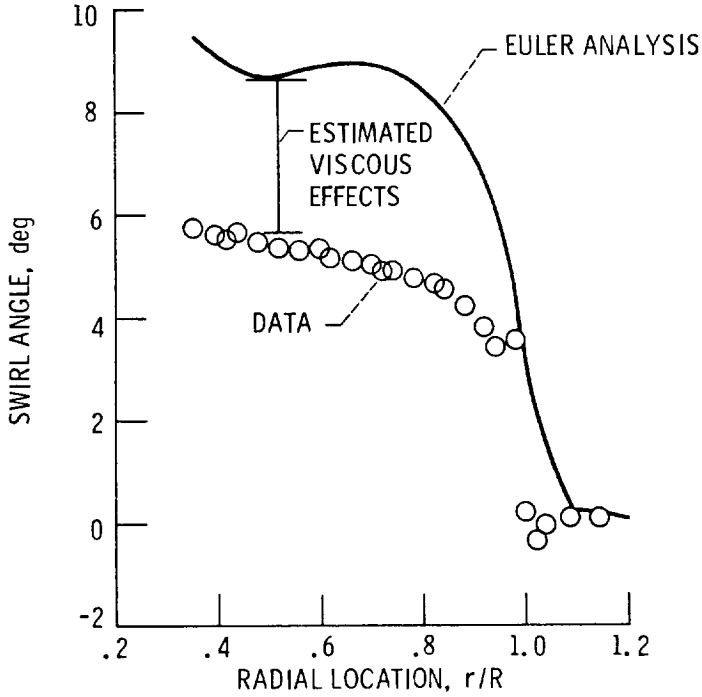

Figure 20. - Comparison of predicted and measured swirl angle downstream of the SR-3 propeller blade. Axial location, 0.21 diameters downstream of the pitch change axis; free stream Mach number, 0.8; advance ratio, 3.06; blade angle at three-quarter radius, 60.5^{0}.

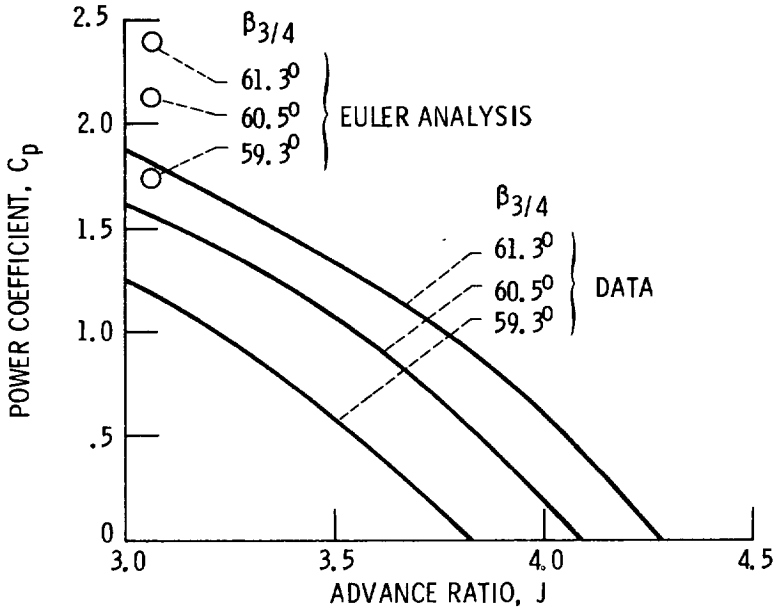

Figure 21. - Comparison of predicted and measured power coefficient for the SR-3 propeller. Free-stream Mach number, 0.8; advance ratio, 3.06.

	APPROACH		STATUS
	STEADY AERODYNAMICS	PROPAGATION	
(A)	LIFTING LINE/2D AIRFOIL (SR)	LINEAR - TIME DOMAIN	CURRENT
(B)	3D NON-LINEAR (SR)	LINEAR - TIME DOMAIN	CURRENT
(C)	LIFTING LINE/2D AIRFOIL (CR)	LINEAR - TIME DOMAIN	IN DEVELOPMENT
(D)	3D EXACT LINEAR (SR)	LINEAR - FREQUENCY DOMAIN	IN DEVELOPMENT
(E)	3D NON-LINEAR (SR)	LINEAR - FREQUENCY DOMAIN	IN DEVELOPMENT
(F)	3D NON-LINEAR (SR)	NON-LINEAR/LINEAR	IN DEVELOPMENT
	UNSTEADY AERODYNAMICS		
(G)	3D EXACT LINEAR (SR)	LINEAR - FREQUENCY DOMAIN	IN DEVELOPMENT
(H)	LINEAR LIFT RESPONSE-ACTUATOR DISK (SR)	LINEAR - FREQUENCY DOMAIN	IN DEVELOPMENT

Figure 22. - Acoustic Analysis Methods.

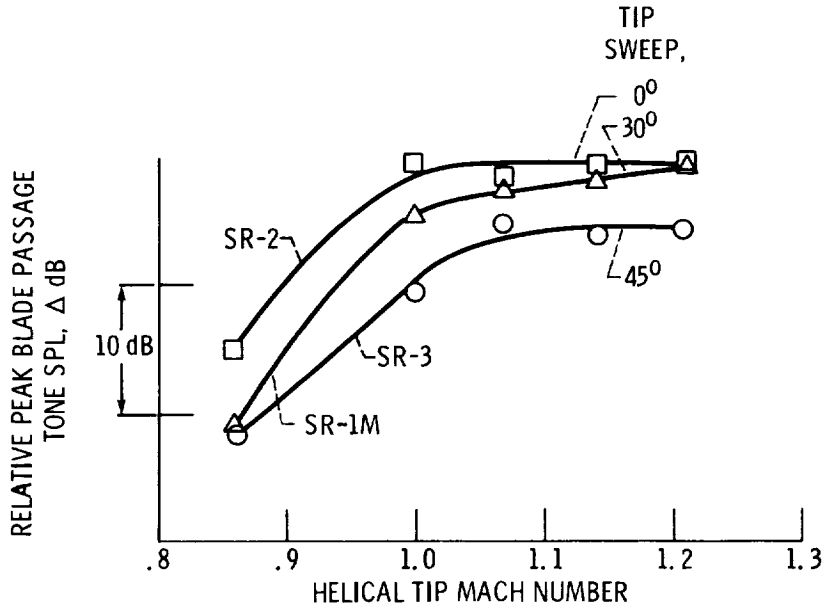

Figure 23. - Maximum blade passage tone variation with helical tip Mach number for 8-bladed propellers. (All at nominal advance ratio of 3.06.)

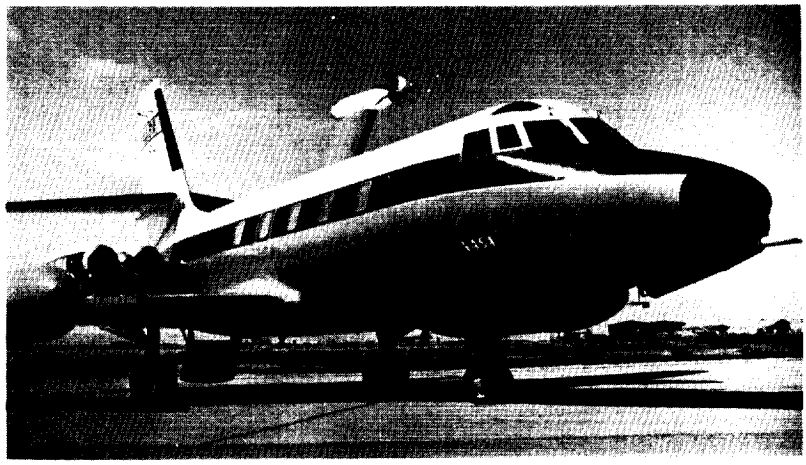

Figure 24. - Photograph of SR-3 propeller installed on the Jetstar aircraft for in flight noise measurements.

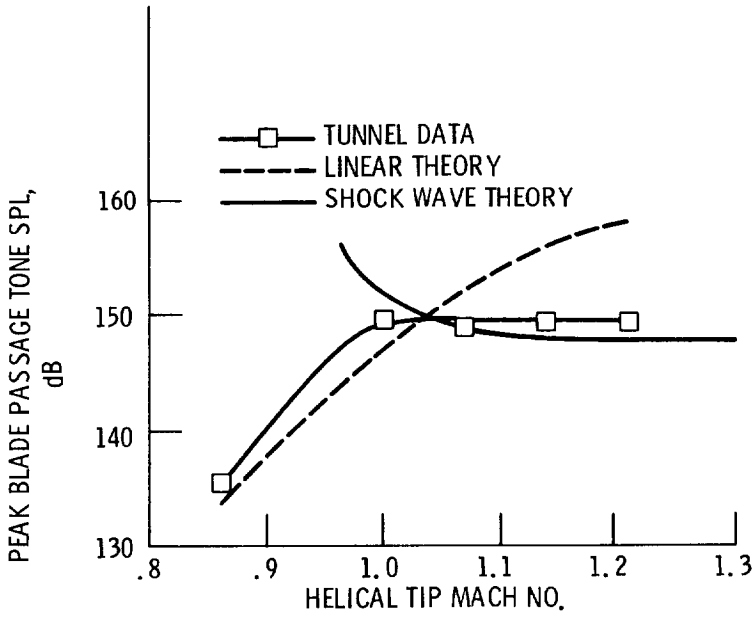

Figure 25. - Near field noise of the 8-bladed 0^{0} swept propeller (SR-2) at 1.5 diameters from propeller tip.

Figure 26. - Photograph of the SR-3 (8 bladed, 45^{0} swept) propeller installed for wing effects acoustic tests in the Lewis 8-by-6 foot wind tunnel.

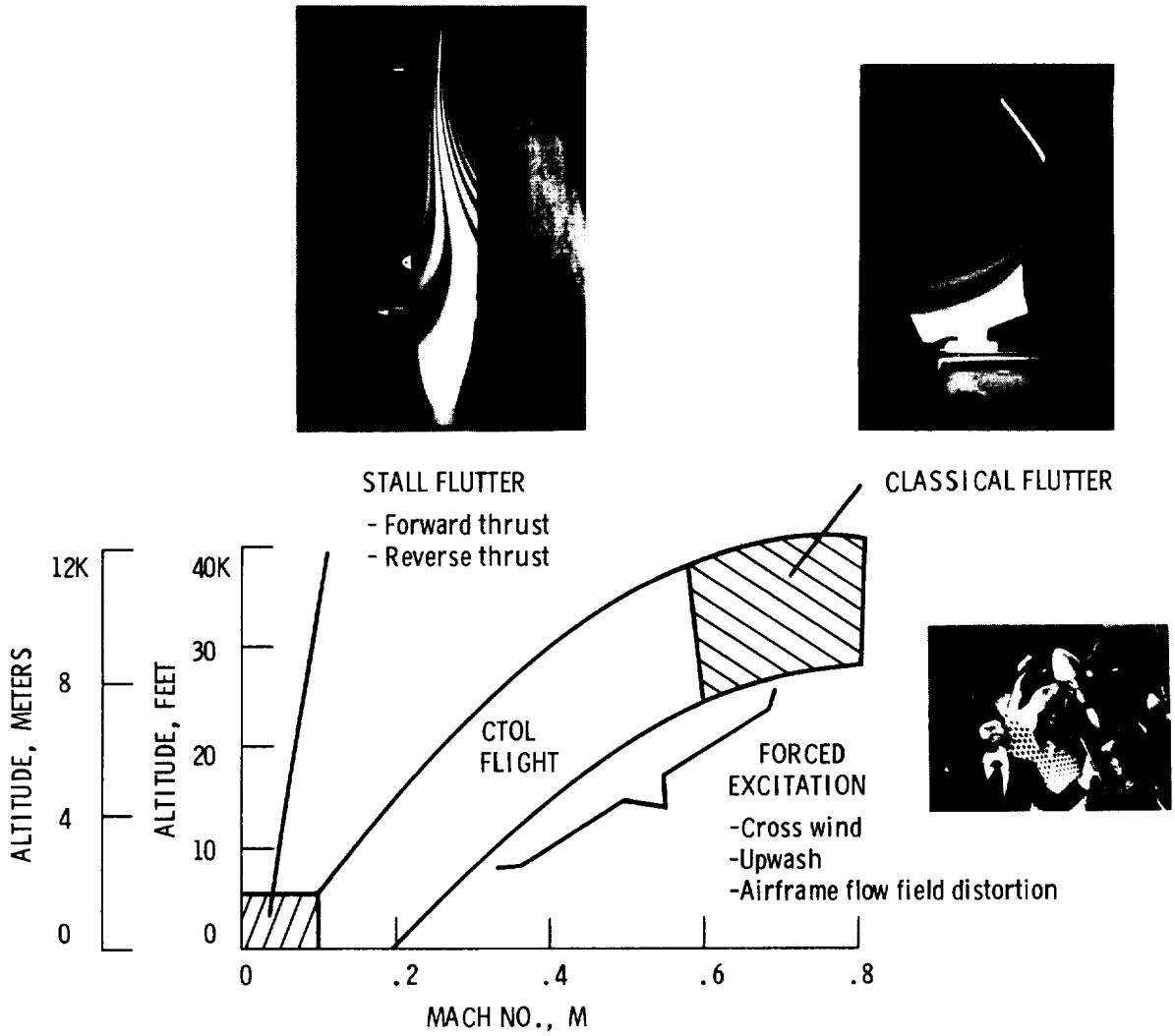

Figure 27. - Areas of propeller aeroelastic research.

	METHOD	STATUS
	STRUCTURAL BLADE MODELS	
(A)	SWEPT STRAIGHT BEAM	CURRENT
(B)	SWEPT CURVED BEAM	IN DEVELOPMENT
(C)	PLATE FINITE ELEMENT	IN DEVELOPMENT
	UNSTEADY AERODYNAMIC MODELS	
	FORCED EXCITATION	
(D)	2D QUASI-STEADY	CURRENT
	STALL FLUTTER	
(E)	EMPIRICAL SUBSONIC AIRFOIL	CURRENT
	CLASSICAL FLUTTER	
(F)	2D SUB AND SUPERSONIC CASCADE	CURRENT
(G)	2D TRANSONIC AIRFOIL	CURRENT
(H)	2D SUBSONIC AIRFOIL	CURRENT
(I)	3D SUBSONIC CASCADE	IN DEVELOPMENT

Figure 28. - Propeller aeroelastic analysis methods.

Figure 29. - Photograph of the SR-2C (8-bladed, 0^{0} sweep) propeller installed on the semi-span aircraft model in the Ames 14-foot transonic wind tunnel.

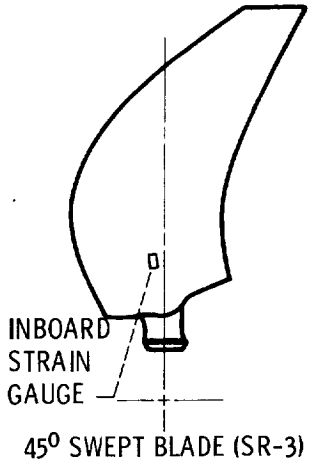

INBOARD STRAIN GAGE 1P STRESS MEAS/PRED

SWEEP	ISOLATED	INSTALLED
0°	~1	~0.4/0.8
45°	~1.6	(FUTURE)
60°	~1.5	--

Figure 30. - Propeller forced excitation results at Mach 0.8.

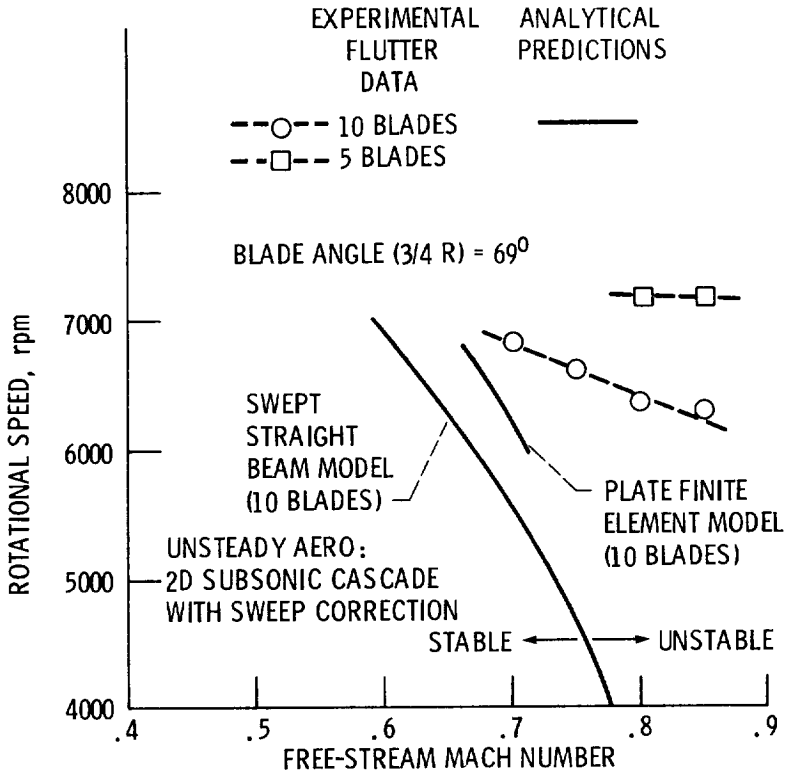

Figure 31. - A comparison of predicted and measured classical flutter boundaries of the 60° swept propeller model (SR-5).

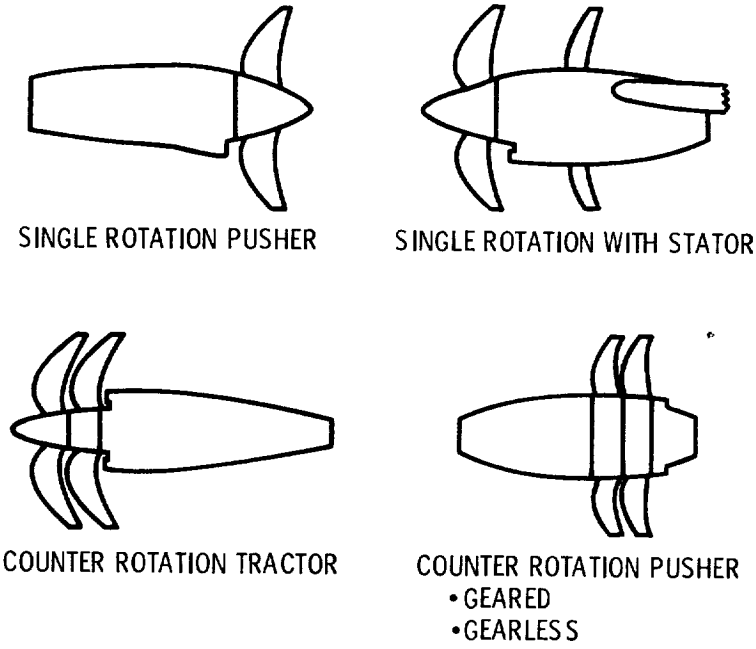

Figure 32. - Future advanced turboprop concepts.

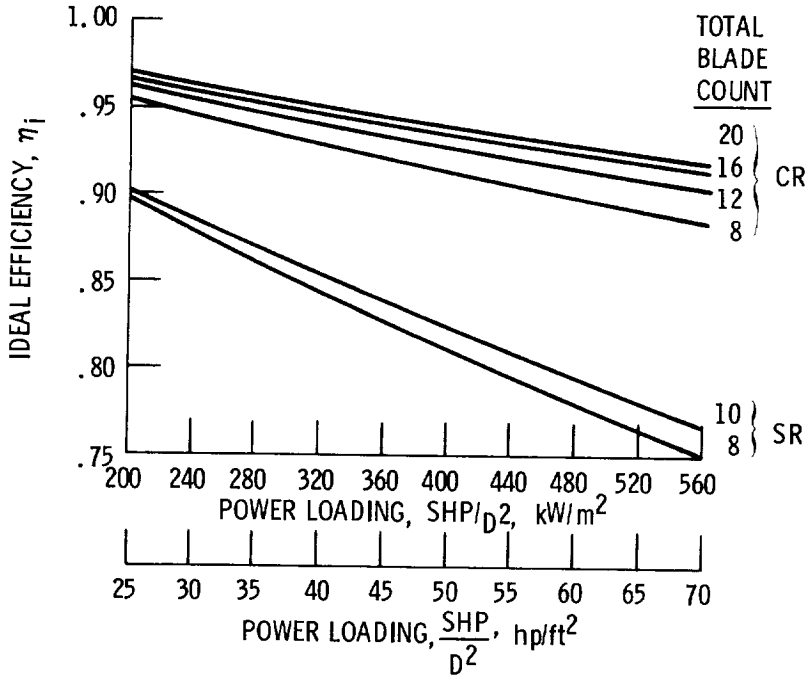

Figure 33. - Comparison of ideal efficiency for single- and counter-rotation propellers: Mo = 0.8, altitude = 10.668 km (35 000 ft), tip speed = 244 m/sec (800 ft/sec).

ADVANCED CR PROPELLER

$\Delta \eta_{CRP-SRP}$ +8 PTS

Δ PROPELLER WEIGHT +17 %

Δ CRUISE NOISE +1.6 dBA

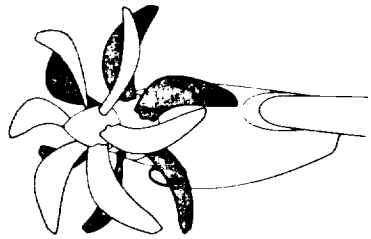

DIFFERENTIAL PLANETARY GEARBOX

Δ GB WEIGHT -15 %

Δ EFFICIENCY +.2 %

Δ ACQUISITION COST +19 %

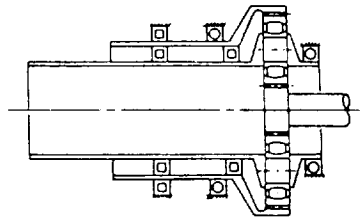

OVERALL INSTALLATION

Δ FUEL	-9 %
Δ DOC	-2.9 %
Δ CABIN ACOUSTIC TREATMENT	+5 %
Δ AIRCRAFT INSTALLATION LOADS (PROP GYRO MOMENT AND DRIVE TORQUE)	-80 TO -100 %

Figure 34. - Advanced counter-rotation propeller potential.

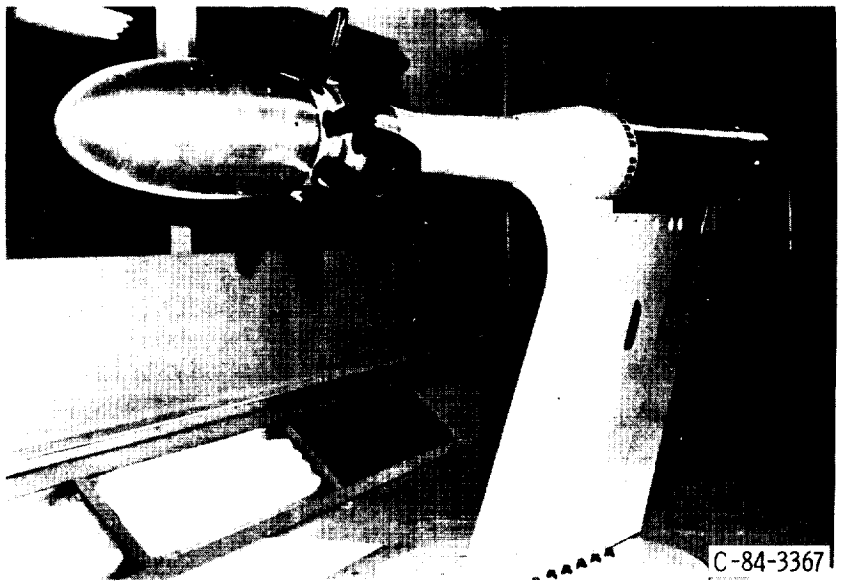

Figure 35. - Test model of the 16-bladed gearless pusher CR propeller.

1. Report No.	2. Government Accession No.	3. Recipient's Catalog No.
NASA TM-83733		

4. Title and Subtitle	5. Report Date
Summary of Recent NASA Propeller Research	
	6. Performing Organization Code: 505-40-32

7. Author(s)	8. Performing Organization Report No.
Daniel C. Mikkelson, Glenn A. Mitchell and Lawrence J. Bober	E-2216
	10. Work Unit No.

9. Performing Organization Name and Address	11. Contract or Grant No.
National Aeronautics and Space Administration Lewis Research Center Cleveland, Ohio 44135	
	13. Type of Report and Period Covered: Technical Memorandum

12. Sponsoring Agency Name and Address	14. Sponsoring Agency Code
National Aeronautics and Space Administration Washington, D.C. 20546	

15. Supplementary Notes

Prepared for the AGARD Fluid Dynamics Panel Meeting on Aerodynamics and Acoustics of Propellers, Toronto, Canada, October 1-4, 1984.

16. Abstract

Advanced high-speed propellers offer large performance improvements for aircraft that cruise in the Mach 0.7 to 0.8 speed regime. At these speeds, studies indicate that there is a 15 to near 40 percent block fuel savings and associated operating cost benefits for advanced turboprops compared to equivalent technology turbofan powered aircraft. The current status of the NASA research program on high-speed propeller aerodynamics, acoustics, and aeroelastics is described. Recent wind tunnel results for five eight- to ten-blade advanced models are compared with analytical predictions. Test results show that blade sweep was important in achieving net efficiencies near 80 percent at Mach 0.8 and reducing near-field cruise noise by about 6 dB. Lifting line and lifting surface aerodynamic analysis codes are under development and some results are compared with propeller force and probe data. Also, analytical predictions are compared with some initial laser velocimeter measurements of the flow field velocities of an eight-bladed 45° swept propeller. Experimental aeroelastic results indicate that cascade effects and blade sweep strongly affect propeller aeroelastic characteristics. Comparisons of propeller near-field noise data with linear acoustic theory indicate that the theory adequately predicts near-field noise for subsonic tip speeds but overpredicts the noise for supersonic tip speeds. A study of advanced counter-rotation turboprops indicates that there may be about a 9 percent additional block fuel savings compared to a single rotation systems at Mach 0.8.

17. Key Words (Suggested by Author(s))	18. Distribution Statement
Propellers; Turboprop; Propulsion; Analysis; Aeroelasticity; Propeller noise	Unclassified - unlimited STAR Category 01

19. Security Classif. (of this report)	20. Security Classif. (of this page)	21. No. of pages	22. Price*
Unclassified	Unclassified		

*For sale by the National Technical Information Service, Springfield, Virginia 22161

National Aeronautics and
Space Administration

Washington, D.C.
20546

Official Business
Penalty for Private Use, $300

SPECIAL FOURTH CLASS MAIL
BOOK

Postage and Fees Paid
National Aeronautics and
Space Administration
NASA-451

NASA

POSTMASTER: If Undeliverable (Section 158
Postal Manual) Do Not Return